The Atmospheric Response to Weak Sea Surface Temperature Fronts*

NIKLAS SCHNEIDER

International Pacific Research Center, and Department of Oceanography, University of Hawai'i at Mānoa, Honolulu, Hawaii

BO QIU

Department of Oceanography, University of Hawai'i at Mānoa, Honolulu, Hawaii

(Manuscript received 17 July 2014, in final form 27 April 2015)

ABSTRACT

The response of the atmospheric boundary layer to fronts of sea surface temperature (SST) is characterized by correlations between wind stress divergence and the downwind component of the SST gradient and between the wind stress curl and the crosswind component of the SST gradient. The associated regression (or coupling) coefficients for the wind stress divergence are consistently larger than those for the wind stress curl. To explore the underlying physics, the authors introduce a linearized model of the atmospheric boundary layer response to SST-induced modulations of boundary layer hydrostatic pressure and vertical mixing in the presence of advection by a background Ekman spiral. Model solutions are a strong function of the SST scale and background advection and recover observed characteristics. The coupling coefficients for wind stress divergence and curl are governed by distinct physics. Wind stress divergence results from either large-scale winds crossing the front or from a thermally direct, cross-frontal circulation. Wind stress curl, expected to be largest when winds are parallel to SST fronts, is reduced through geostrophic spindown and thereby yields weaker coupling coefficients.

1. Introduction

Satellite-borne observations of the atmospheric response to fronts of sea surface temperature (SST) have revolutionized the understanding of midlatitude air–sea interaction (Xie 2004; Small et al. 2008). While the traditional, large-scale view holds that the ocean primarily responds to forcing by the atmosphere, the ocean mesoscale shows a ubiquitous imprint of SST fronts on the atmospheric boundary layer (Chelton and Xie 2010; Xie 2004). For scales shorter than about 1000 km, wind speeds are proportional to SST perturbations, and wind stress divergence and curl are proportional to the downwind and crosswind gradients of SST, respectively (O'Neill et al. 2003; Chelton and Xie 2010; Song et al. 2009). The associated regression coefficients (i.e., coupling coefficients) vary seasonally and regionally, but the coupling coefficients between divergence and downwind SST gradients are consistently larger than those between wind stress curl and crosswind SST gradients in observations (Chelton and Xie 2010) and in high-resolution numerical models (Seo et al. 2007; Song et al. 2009; Bryan et al. 2010). Kinematically, this results from gradients of the frontally induced surface stress direction that diminish the wind stress curl but enhance the wind stress divergence (O'Neill et al. 2010a). Here, we seek to dynamically explain these observations using a linearized model for the atmospheric boundary layer that includes advection by background Ekman winds, frontally induced air–sea fluxes of heat, and their impact on the momentum budget. In the process, we provide a unified framework for all processes put forth in the context of frontal air–sea interaction, cast frontal air–sea interaction as a classical Rossby adjustment problem, and explore its scale and parameter dependence.

Denotes Open Access content.

* International Pacific Research Center Publication Number 1119 and School of Ocean and Earth Science and Technology Publication Number 9423.

Corresponding author address: N. Schneider, International Pacific Research Center, University of Hawai'i at Mānoa, 1680 East West Road, Honolulu, HI 96822.
E-mail: nschneid@hawaii.edu

DOI: 10.1175/JAS-D-14-0212.1

Two mechanisms are invoked to explain the response of boundary layer winds and surface stresses to fronts of SST: adjustments of vertical mixing and of baroclinic pressure gradients. Modulation of air–sea temperature fluxes affects vertical mixing between winds near surface and aloft and accelerate (decelerate) surface winds downstream of a cold-to-warm (warm-to-cold) front (Wallace et al. 1989; Hayes et al. 1989). The increase in vertical mixing and associated deepening of the boundary layer may be limited to the wake of the non-equilibrated difference of boundary layer and sea surface temperatures, or it may extend farther downstream if the boundary layer depth is permanently altered (Samelson et al. 2006). Support for this process comes from observations of higher surface winds (Sweet et al. 1981) and deep boundary layers on the warm side of SST fronts (Businger and Shaw 1984; Wai and Stage 1989).

Air–sea temperature fluxes downstream of an SST front also imprint the oceanic conditions on the hydrostatic, baroclinic pressure in the boundary layer (Lindzen and Nigam 1987). Evidence for this pressure effect comes from the covariations of divergences of surface winds and surface wind stress with the Laplacian of surface temperature and sea level pressure (Shimada and Minobe 2011; Tokinaga et al. 2009; Lambaerts et al. 2013).

The distinct responses of the wind stress divergence and curl emerge from the response of the atmospheric boundary layer momentum, heat, and mass balances to the accelerations induced by vertical mixing and pressure gradient mechanisms. In the absence of horizontal advection, Ekman pumping due to the divergence of the frontally induced Ekman transports displaces the stratification outside of the boundary layer and generates a back pressure in the boundary layer (Lindzen and Nigam 1987; Battisti et al. 1999) that spins down (Greenspan and Howard 1963; Holton 1965a,b; Pedlosky 1967) the wind stress curl.[1] Atmospheric observations show the back pressure, in that frontal adjustments extend beyond the boundary layer and partially offset the surface pressure gradients induced by mesoscale SST (Hashizume et al. 2002). A series of numerical investigations on the response of the free troposphere to SST fronts relies on this frontally induced Ekman pumping to couple the boundary layer with the atmosphere aloft (Feliks et al. 2004, 2007, 2011). In these studies, the atmospheric boundary layer temperature is assumed to be in equilibrium with the underlying SST, and the stress results from a one-dimensional momentum budget in the boundary layer in response to the frontally induced baroclinic and back pressures. The role of advection that leads to imbalances of boundary layer temperature and SST and that affects the boundary layer momentum budget is not considered.

Recent modeling studies (Kilpatrick 2013; Kilpatrick et al. 2014) that build upon the two-dimensional simulations of frontal air–sea interaction (Wai and Stage 1989; Spall 2007) show the dynamics of frontal interaction to be a strong function of the large-scale wind magnitude and direction relative to the front. For strong cross-frontal winds, the effective time scale of an air column crossing the front is shorter than an inertial period. Resulting boundary layer transport divergences excite vertically propagating gravity waves in the free troposphere (Kilpatrick et al. 2014). In contrast, for alongfront winds, the effective time scale experienced by an air column that crosses the front is longer than an inertial period so that a surface trapped response results consistent with a spindown of the lower troposphere induced by the frontally induced secondary circulation (Kilpatrick 2013).

In this manuscript, we explore the hypothesis that spindown is responsible for the consistently smaller magnitude of the coupling coefficients for the wind stress curl than for the wind stress divergence. To this end, we adopt a reduced-gravity model for the atmospheric boundary layer (Lindzen and Nigam 1987; Battisti et al. 1999) to include advection by a prescribed, uniform, geostrophic wind and forcing by an arbitrary SST distribution (sections 2 and 3). We explore the responses of the model vis-à-vis observed characteristics (section 4), and show the distinct dynamics governing the wind stress divergence and curl and their coupling coefficients (section 5). Parameter sensitivity of the results and a comparison with observations are presented (section 6), followed by conclusions (section 7).

2. Reduced-gravity model

We employ a minimal model that includes the frontal physics outlined above and simplifies the vertical structure of the lower atmosphere as an active layer adjacent to the surface separated by a sharp inversion from the resting troposphere aloft (Battisti et al. 1999). The full, nondimensional equations are formulated on an f plane using classical scaling and are then linearized about a background Ekman spiral due to a prescribed, geostrophic wind.

The active layer of depth h is capped by an inversion with potential temperature jump $\Delta\Theta$ and a reduced gravity $g' = (\Delta\Theta/\Theta_0)g$, where g is Earth's gravitational acceleration, and Θ_0 is a reference boundary layer potential temperature. This active layer is forced by prescribed, constant, barotropic, geostrophic wind with a lateral scale far larger

[1] This effect is called "buoyancy shutdown" in the oceanic bottom boundary layer (MacCready and Rhines 1991) and drastically reduces bottom friction (Benthuysen 2010).

than the frontal circulation and sea surface temperature T. We consider the system in steady state, restricting time scales to longer than the maximum of an inertial period, the spindown time scale (see below), and the thermal adjustment time of the layer.

Equations and variables are nondimensionalized using the Rossby radius $\sqrt{g'H}/f$ as a horizontal scale, with f the Coriolis frequency, the mean inversion height H as the vertical scale, and the gravity wave speed $\sqrt{g'H}$ as the horizontal velocity scale (Table A1). Scales for boundary layer potential temperatures and sea surface temperature are $\Delta\Theta$. In the vertical, we use a sigma coordinate $s = z/h$, where z is the vertical distance, so that $s = 0$ is the sea surface, and $s = 1$ is the time-dependent inversion height.

With our emphasis on the wind response, we assume that the potential temperature in the boundary layer is constant in the vertical and solve for the winds and shear. Our approach is a counterpoint to models of the stratocumulus boundary layer that resolve the subcloud and cloud layers but prescribe the winds (Schubert et al. 1979a), and it is consistent with numerical results of Small et al. (2005) and the deeper vertical penetration of frontally induced air temperature compared to wind variations (O'Neill et al. 2010b). The heat budget

$$\overline{\mathbf{u}} \cdot \nabla\Theta = -h^{-1}\gamma_\Theta(\Theta - T) + A_h\nabla^2\Theta \tag{1}$$

balances advection of temperature Θ by vertically averaged, horizontal wind $\overline{\mathbf{u}}$ with the combined turbulent and radiative flux of heat taken to be proportional to the difference of boundary layer temperature and the sea surface temperature T with an adjustment rate γ_Θ. Overbars denote vertical averages. Lateral mixing with coefficient A_h is introduced to capture, albeit primitively, the damping by the sea breeze of the lateral gradients of temperature for scales smaller than a Rossby radius of deformation.

The horizontal momentum budget for a Boussinesq fluid (see the appendix for a detailed derivation)

$$\begin{aligned} &h\mathbf{u}\cdot\nabla\mathbf{u} + w^\star\partial_s\mathbf{u} + h\hat{\mathbf{e}}_3 \times (\mathbf{u} - \mathbf{U}_g) \\ &\quad = -g^\star h\nabla h + h^2(1-s)\nabla\Theta + h^{-1}\partial_s E\partial_s\mathbf{u} \end{aligned} \tag{2}$$

balances on the left-hand side horizontal and vertical advection and the Coriolis accelerations, with right-hand-side forces associated with the pressure gradient due to the inversion height variations and gradients of boundary layer temperature and with the vertical divergence of the turbulent momentum fluxes. The response is governed by the large-scale, background geostrophic wind $\mathbf{U}_g = U_g\hat{\mathbf{e}}_g$, with direction given by unit vector $\hat{\mathbf{e}}_g$ and magnitude U_g that corresponds to a geostrophic Froude number, by the Ekman number

$$E = \frac{A}{fH^2}, \tag{3}$$

with A being the vertical exchange coefficient that, in general, is a function of s, and by the reduced gravity

$$g^\star = 1 - \Theta \tag{4}$$

that includes the impacts of the varying temperature in the boundary layer.

The continuity equation

$$\nabla\cdot(h\mathbf{u}) + \partial_s w^\star = 0 \tag{5}$$

determines the sigma vertical velocity

$$w^\star = w - s\mathbf{u}\cdot\nabla h \tag{6}$$

as the residual of the divergence of the boundary layer winds and advection of inversion height changes. The sea surface and inversion are material surfaces so that

$$w^\star = 0 \quad \text{at} \quad s = 0, 1. \tag{7}$$

At the sea surface $s = 0$, horizontal winds equal ocean currents, which we assume to be zero:

$$\mathbf{u} = 0 \quad \text{at} \quad s = 0 \tag{8}$$

so that the surface stress $\boldsymbol{\tau} = E\partial_s\mathbf{u}|_{s=0}$ depends on the near-surface wind shear. This is equivalent to a linear drag law for surface stress

$$\boldsymbol{\tau} = \frac{E}{s_0}\mathbf{u}|_{s_0} \quad \text{at} \quad s = 0, \tag{9}$$

with a drag coefficient E/s_0 determined by the surface value of E and near-surface winds evaluated at $s = s_0$, the top of the surface layer. At the inversion $s = 1$, turbulent fluxes vanish:

$$E\partial_s\mathbf{u} = 0 \quad \text{at} \quad s = 1, \tag{10}$$

which implies for $E \neq 0$ a vanishing vertical shear of the background wind.

The mixing mechanism (Wallace et al. 1989; Hayes et al. 1989) implies a dependence of E on the surface stability $\delta = T - \Theta$, the difference of sea surface temperature and boundary layer temperature at the lowest level above the sea surface:

$$E = E(\delta), \tag{11}$$

which increases (decreases) turbulent E for unstable, $\delta > 0$ (stable, $\delta < 0$) air–sea temperature differences. In

the interest of brevity, we disregard wind speed dependencies of the surface value of E and drag coefficient in Eq. (9) that are responsible for differences in coupling coefficients between SST and wind speed and stress (O'Neill et al. 2012). Their consideration would render coefficients of the frontal responses, introduced below, a function of background wind speed but would otherwise not change results.

3. Linearization for small-amplitude mesoscale sea surface temperature variations

To obtain solutions of the winds and temperatures in the active layer, we expand dependent variables in powers of ε, where ε^0 denotes large-scale background state and frontally induced components are of order ε^1:

$$(T,\mathbf{u},\Theta,h,w,\boldsymbol{\tau},g^{\star},E)=[T^{(0)},\mathbf{u}^{(0)},\Theta^{(0)},h^{(0)},w^{\star(0)},\boldsymbol{\tau}^{(0)},g^{\star(0)},E^{(0)}]+\varepsilon[T^{(1)},\mathbf{u}^{(1)},\Theta^{(1)},h^{(1)},w^{\star(1)},\boldsymbol{\tau}^{(1)},g^{\star(1)},E^{(1)}]+\cdots, \tag{12}$$

and we assume that the frontally induced circulation is sufficiently weak to allow a linearization in ε. The condition of small ε is satisfied if first-order winds are small compared to background fields [i.e., $|\mathbf{u}^{(1)}|\ll|\mathbf{u}^{(0)}|$, and if $E^{(1)}\ll E^{(0)}$]. Scaling of the frontally induced winds via a nonrotating balance of the pressure gradient and vertical mixing implies that the frontally induced pressure gradient has to be small compared to the background surface stress $|\nabla T^{(1)}|\ll|\boldsymbol{\tau}^{(0)}|$.

a. Background Ekman spiral

We assume a scale separation between background state and frontally induced circulation so that the background forcing $\mathbf{U}_g$ and $T^{(0)}$ are independent of the horizontal coordinate $\mathbf{x}$. To order ε^0 the circulation is an Ekman spiral. Gradients vanish so that the vertical velocity is identically zero and the inversion height is undisturbed:

$$w^{\star(0)}=0 \quad \text{and} \tag{13}$$

$$h^{(0)}=1. \tag{14}$$

The boundary layer temperature $\Theta^{(0)}$ equals the background sea surface temperature $T^{(0)}=0$, which is set, without loss of generality, to zero so that

$$g^{\star(0)}=1. \tag{15}$$

The background surface stability $\delta^{(0)}=0$, and the vertical exchange coefficient is $E^{(0)}=E[\delta^{(0)}]$.

The horizontal winds form an Ekman spiral in the bottom Ekman layer:

$$\hat{\mathbf{e}}_3\times[\mathbf{u}^{(0)}-\mathbf{U}_g]=\partial_s E^{(0)}\partial_s\mathbf{u}^{(0)}, \tag{16}$$

with boundary conditions

$$E^{(0)}\partial_s\mathbf{u}^{(0)}=0 \quad \text{at} \quad s=1 \tag{17}$$

and a surface stress from Eq. (9)

$$\boldsymbol{\tau}^{(0)}=\frac{E^{(0)}}{s_0}\mathbf{u}|_{s_0}^{(0)} \quad \text{at} \quad s=0. \tag{18}$$

b. Sea surface temperature–induced circulation

The order ε of the heat budget Eq. (1)

$$\overline{\mathbf{u}^{(0)}}\cdot\nabla\Theta^{(1)}=\gamma_\Theta[T^{(1)}-\Theta^{(1)}]+A_h\nabla^2\Theta^{(1)} \tag{19}$$

balances horizontal advection by the vertically averaged background winds with the air–sea fluxes and lateral mixing. The frontally induced atmospheric temperatures $\Theta^{(1)}$ are independent of the frontally induced winds and inversion height but determine the forcing of the order ε momentum and continuity equations. These extend the classic, forced, shallow water equations (Gill 1982) to frontal air–sea interaction and include horizontal advection by the background winds and vertical displacement by frontally induced updrafts of the background Ekman spiral, the Coriolis acceleration, mixing by the background eddy viscosity, and the back pressure due to gradients of inversion height:

$$\underbrace{\mathbf{u}^{(0)}\cdot\nabla\mathbf{u}^{(1)}+w^{\star(1)}\partial_s\mathbf{u}^{(0)}}_{\text{Advection}}+\underbrace{\hat{\mathbf{e}}_3\times\mathbf{u}^{(1)}}_{\text{Coriolis}}+\underbrace{\nabla h^{(1)}}_{\text{Back pressure}}-\underbrace{\partial_s E^{(0)}\partial_s\mathbf{u}^{(1)}}_{\text{Background mixing}}=\mathbf{F}, \tag{20}$$

where we have used Eq. (15).

The SST-induced forcing $\mathbf{F}$

$$\mathbf{F} = \underbrace{(1-s)\nabla\Theta^{(1)}}_{\text{Baroclinic pressure}} + \underbrace{\delta^{(1)}\partial_s\left[\left.\frac{d\ln E}{d\delta}\right|_{\delta^{(0)}} E^{(0)}\partial_s\mathbf{u}^{(0)}\right]}_{\text{Vertical mixing effect}} \tag{21}$$

consists of the baroclinic pressure gradient (Lindzen and Nigam 1987) and of the vertical mixing effect (Wallace et al. 1989; Hayes et al. 1989; Samelson et al. 2006). The latter vertically redistributes background momentum in response to frontally altered stability $\delta^{(1)} = T^{(1)} - \Theta^{(1)}$ that changes vertical mixing $E^{(1)} = (dE/d\delta)|_{\delta^{(0)}}\delta^{(1)}$. The linearization of the total vertical turbulent flux of horizontal momentum (Koseki and Watanabe 2010) thus consists of two components: the vertical mixing effect in Eq. (21) and the background mixing of frontally induced winds in Eq. (20).

The continuity equation

$$\mathbf{u}^{(0)}\cdot\nabla h^{(1)} + \nabla\cdot\mathbf{u}^{(1)} + \partial_s w^{\star(1)} = 0 \tag{22}$$

balances to order ε the advection of the inversion height by the background wind with the divergence of the frontally induced horizontal winds and updrafts. Boundary conditions

$$\begin{aligned} &\mathbf{u}^{(1)} = 0, \quad w^{\star(1)} = 0 \quad \text{at} \quad s = 0 \quad \text{and} \\ &E^{(0)}\partial_s\mathbf{u}^{(1)} + E^{(1)}\partial_s\mathbf{u}^{(0)} = 0, \quad w^{\star(1)} = 0 \quad \text{at} \quad s = 1 \end{aligned} \tag{23}$$

imply that boundary layer transport divergences are balanced by inversion height advection by background transports. From Eq. (9), the surface stress

$$\boldsymbol{\tau}^{(1)} = \frac{E^{(0)}}{s_0}\mathbf{u}|_{s_0}^{(1)} + \frac{E^{(1)}}{s_0}\mathbf{u}|_{s_0}^{(0)} \tag{24}$$

consists of contributions due to background mixing acting on the frontally induced surface winds and the surface stress due to the vertical mixing effect.

c. Dynamical regimes

Equations (19)–(22) with boundary conditions Eq. (23) and the specification of E up to order ε form a linear system for the dependent variables $\Theta^{(1)}$, $\mathbf{u}^{(1)}$, $w^{\star(1)}$, and $h^{(1)}$ forced by a mesoscale sea surface temperature field $T^{(1)}$ and background Ekman spiral $\mathbf{u}^{(0)}$. Coefficients are $\mathbf{x}$ independent, and equations are expanded in a Fourier series $\exp[\imath(\mathbf{k}\cdot\mathbf{x})]$, with $\imath = \sqrt{-1}$. For every horizontal wavenumber $\mathbf{k}$, the vertical s dependence is solved and yields the Fourier coefficients, marked by a tilde, as a convolution of the transfer functions $\tilde{\mathbf{R}}$ and Fourier components of $T^{(1)}$:

$$\tilde{\Upsilon}^{(1)} = \tilde{\mathbf{R}}_\Upsilon\tilde{T}^{(1)}, \tag{25}$$

where Υ is any of the dependent variables. Real and imaginary parts of $\tilde{\mathbf{R}}_\Upsilon$ correspond to in-phase and out-of-phase relationships, respectively, between $\tilde{\Upsilon}^{(1)}$ and $\tilde{T}^{(1)}$.

The character of the solution is determined by the length scales of the thermal wake and the Froude number. Comparing in Eq. (19) the air–sea heat flux with the background advection or the lateral mixing term yields the downwind wavenumber component $k_{\text{ad}}^{-1} = \gamma_\Theta^{-1}|\overline{\mathbf{u}^{(0)}}|$ and $k_{\text{Ah}}^{-2} = \gamma_\Theta^{-1}A_h$. For wavelengths shorter than the downwind displacement k_{ad}^{-1} but larger than the lateral mixing length k_{Ah}^{-1}, for example for strong cross-frontal winds, advection dominates the air–sea fluxes, and $\tilde{\Theta}$ is small and out of phase with SST, leading to a wake of elevated air–sea temperature differences downstream of a sharp SST front. For wavelengths larger than k_{ad}^{-1}, for example for along-frontal winds, boundary layer temperatures approach SSTs. In this case, gradients of boundary layer temperature and hydrostatic pressure reflect those of SSTs and become identical in the fast thermal adjustment limit $\gamma_\Theta^{-1} = 0$ considered by Feliks et al. (2004). Beyond a high wavenumber cutoff k_{Ah}^{-1}, lateral mixing balances of air–sea fluxes and maintains nonequilibrium values of stability.

The scale k_{ad}^{-1} informs the relative roles of the baroclinic pressure gradient forcing and vertical mixing effect in Eq. (21) that have been the subject of a number of investigations (Minobe et al. 2010; Shimada and Minobe 2011; Takatama et al. 2012). For scales larger than those affected by lateral mixing, the relative magnitude of the components of $\mathbf{F}$ in Eq. (21) is

$$O\left[\frac{\delta^{(1)}\partial_s\dfrac{d\ln E}{d\delta}\boldsymbol{\tau}^{(0)}}{(1-s)\nabla\Theta^{(1)}}\right] = k_{\text{ad}}^{-1}\left.\frac{d\ln E}{d\delta}\right|_{\delta^{(0)}}\boldsymbol{\tau}^{(0)}, \tag{26}$$

where we have scaled the stability and temperature gradient with the solution of Eq. (19) for a straight SST front. For zero background winds, accelerations due to frontally induced turbulent mixing vanish, and the baroclinic pressure gradient is the only forcing. As the cross-frontal background winds increase, the downstream wake broadens and reduces the frontally induced baroclinic pressure gradient, while vertical mixing–induced accelerations increase (Small et al. 2008). As background winds rotate from cross- to alongfront, k_{ad}^{-1} decreases so that air temperature and SST are in equilibrium and the baroclinic pressure gradient dominates. In all, the vertical mixing effect increases as the square of the background winds for a cross-frontal wind with a

TABLE 1. Parameters used in the frontal model. Horizontal and vertical length scales in units of Rossby radius of deformation and mean inversion height, respectively; time scales in inertial periods; and temperature as a fraction of mean inversion strength.

		Reference value
	Mixing	
E_0	Ekman depth	0.5
γ	Vertical decay scale of eddy coefficient	0.3
s_0	Surface layer thickness	0.05
$d\ln\gamma/d\delta$	Stability dependence of γ	0.6
$d\ln E_0/d\delta$	Stability dependence of E_0	0.5
γ_Θ^{-1}	Adjustment time of boundary layer temperature	4
A_h	Lateral mixing of temperature	0.014
	SST front	
	Size of doubly periodic domain	50×50
Δ	Cross-frontal width	0.5
B	Wavelength of front in direction of $\hat{\mathbf{e}}_g$	50
δy	Amplitude of frontal undulation, adjusted so background transports $\bar{\mathbf{u}}^{(0)}$ are parallel to front in the alongfront sector	6.4
	SST amplitude	0.1

proportionality factor dependent on the sensitivity of vertical mixing to stability. Lateral mixing of heat impacts length scales smaller than k_{ad}^{-1} and renders temperature and SST in disequilibrium so that the vertical mixing effect remains even for along-frontal background winds.

The response of momentum balance and continuity, Eqs. (20) and (22), to the forcing $\mathbf{F}$ in Eq. (21) represents the final state of a Rossby adjustment and spindown. Its character is well known from the study of mountain waves and the ocean's response to cyclones (Gill 1982; Suzuki et al. 2011), as well as from the time-dependent but nonadvective linear formulation for the diurnal sea breeze (Rotunno 1983; Niino 1987). It is governed by the Froude number of background advective wind $\mathbf{u}^{(0)}$ and the Ekman number E. In the limit of vertically constant advection and vanishing E, subsystems for the boundary layer transport and boundary layer shear exist. The wind shear is independent of the barotropic back-pressure gradient and reduces to a parabolic equation for $w^{\star(1)}$. In contrast, the system for the boundary layer transport and inversion height is hyperbolic for $|\mathbf{k}|^{-1}|\mathbf{k}\cdot\mathbf{u}^{(0)}| > 1$ and supports standing inertia–gravity, Poincaré waves in the lee of an SST disturbance (Spall 2007; Kilpatrick et al. 2014). For $|\mathbf{k}|^{-1}|\mathbf{k}\cdot\mathbf{u}^{(0)}| < 1$, the system is elliptic and yields an evanescent, geostrophic response.

A nonzero E couples the systems for layer shear and transport by the surface stress and yields, in the limit of vanishing advection, a balance of the forcing $\mathbf{F}$ with the Coriolis acceleration and vertical mixing—a frontally induced Ekman circulation in the presence of a thermal wind shear (Cronin and Kessler 2009). In the frontal equivalent of the classical spindown (Greenspan and Howard 1963; Holton 1965a,b; Pedlosky 1967) and buoyancy shutdown (MacCready and Rhines 1991; Benthuysen 2010), convergences of Ekman transports reduce the wind stress curl by adjusting the inversion height gradient (i.e., the back pressure).

4. Response to an undulating front

The frontally induced system is valid for any small-amplitude SST field, including that associated with ocean mesoscale eddies and fronts. To solve for background Ekman spiral and frontally induced circulation, Eqs. (16), (20), and (22) are vertically discretized using first-order finite differences on an equally spaced grid with $10s$ levels. Levels for the vertical velocity and Ekman number include the surface and inversion. Horizontal winds are staggered in between so that surface wind stresses are proportional to the winds at the lowest level adjacent to the surface. The horizontal dependence of SST and Eqs. (19), (20), and (22) are Fourier transformed to horizontal wavenumber space $\mathbf{k}$; the transfer functions $\tilde{\mathbf{R}}$ and Fourier amplitudes of the dependent variables are obtained numerically; and solutions are then transformed back to physical space.

a. Model parameters

The adjustment time of the boundary layer temperature γ_Θ^{-1} is governed by three processes: a fast thermodynamic adjustment of about a day in the subcloud layer, a dynamic adjustment to large-scale divergence on the order of 2 days, and a slower radiative adjustment of 4 days (Schubert et al. 1979b; Bellon and Stevens 2013). We choose the adjustment time of the temperature to be four inertial periods $\gamma_\Theta = 0.25$ (Table 1). The value of A_h is selected to affect only scales smaller than or equal to a Rossby radius of deformation with $\sqrt{A_h/\gamma_\Theta} = 0.24$ (Table 1).

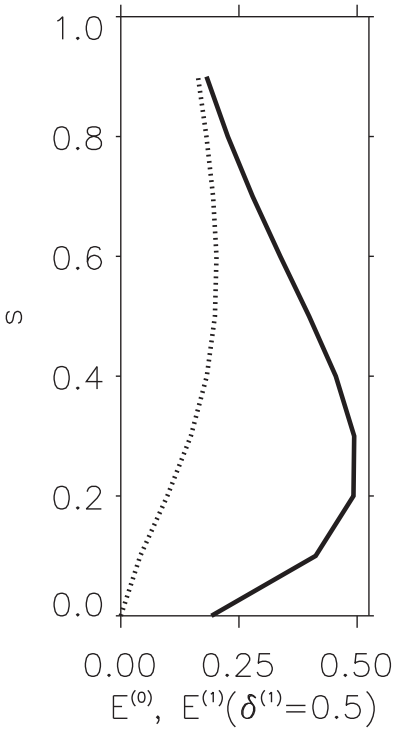

FIG. 1. Background vertical eddy coefficient $E^{(0)}$ (solid line) as a function of the sigma coordinate from the sea surface at $s = 0$ to the inversion at $s = 1$. The dashed line shows the stability-modulated eddy coefficients $E^{(1)}$ for unstable conditions, $\delta^{(1)} = 0.5$.

The Ekman number E has a midlayer maximum, decays toward the surface and the free troposphere (Fig. 1), and mimics the observed structure (Stull 1988; Hong and Pan 1996):

$$E = \frac{s + s_0}{\gamma} E_0 \exp\left(1 - \frac{s + s_0}{\gamma}\right), \tag{27}$$

where s_0 is the thickness of the surface layer, and γ denotes the height $(s + s_0)$ of the maximum value E_0. Guided by the frontal simulation of Kilpatrick et al. (2014), we choose the maximum Ekman number $E_0 = 0.5$ with a decay scale of $\gamma = 0.3$ (Fig. 1).

The modulation of mixing $E(\delta)$ (Wallace et al. 1989; Hayes et al. 1989; Samelson et al. 2006) is obtained by assuming that the maximum eddy coefficients and the vertical decay scale are functions of stability: $E_0 = E_0(\delta)$ and $\gamma = \gamma(\delta)$. In accordance with observations that the frontal modulation of surface roughness is a minor contributor to the modulation of the stress (Small et al. 2008), we choose $E^{(1)} = 0$ at the sea surface $s = 0$. Frontally induced surface stresses in Eq. (24) therefore result only from adjustments of the vertical wind profile. A Taylor expansion of Eq. (27) in δ then yields the frontally induced eddy coefficients

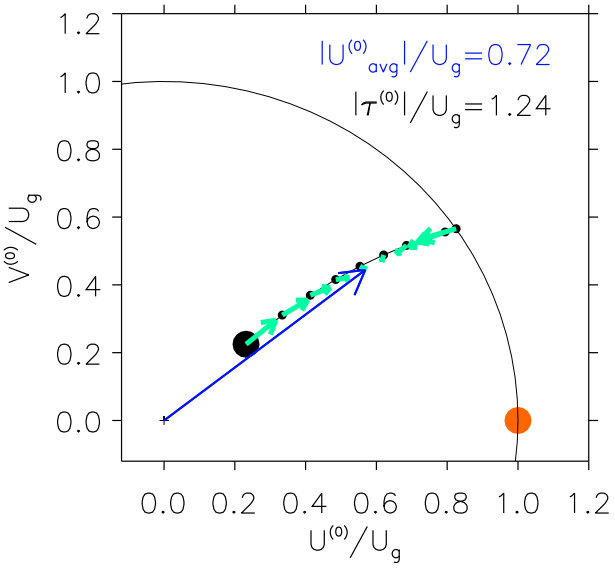

FIG. 2. Background Ekman spiral in the boundary layer in components in directions $\hat{\mathbf{e}}_g$ and $\hat{\mathbf{e}}_3 \times \hat{\mathbf{e}}_g$, aligned and perpendicular to the large-scale geostrophic wind. The value closest to the surface at $s = 0$ is marked by a large black circle; small black circles mark locations farther aloft in sigma coordinate steps of 0.1 to the value adjacent to the inversion. The vertically averaged wind is shown by the blue arrow, and its magnitude is indicated in the upper-right corner. The surface stress is in the direction of near-surface winds, and its magnitude is indicated in the upper-right corner. The acceleration of the frontally induced winds due to unstable air–sea temperature difference is shown by the green arrows. The prescribed geostrophic wind is indicated by the orange dot; all velocities and the stress are normalized by its speed.

$$\left.\frac{d(\ln E)}{d\delta}\right|_{\delta^{(0)}} = \frac{s}{\gamma} \left.\frac{d(\ln\gamma)}{d\delta}\right|_{\delta^{(0)}} \tag{28}$$

as a fraction of $E^{(0)}$ that increases from zero at the sea surface linearly to largest values at the inversion level. The chosen value of $d(\ln\gamma)/d\delta = 0.6$ (Table 1) approximates results of the simulation of Kilpatrick et al. (2014).

b. Background winds

Background winds (Fig. 2) point to the left of the geostrophic wind, are small close to the surface, and approach geostrophic speeds close to the inversion, similar to the classical Ekman spiral with constant eddy coefficients at the bottom of an infinitely deep atmosphere. The vertically averaged wind has a magnitude of 72% of the geostrophic wind, with components in the direction of the geostrophic wind of 57% and in the direction of the prescribed pressure gradient force of 45%. Together with γ_Θ, the downwind thermal wake k_{ad}^{-1} extends 2.89 Rossby radii for a unit value of the prescribed, background geostrophic wind. The surface stress in the direction of the near-surface winds has a magnitude of 1.2 times the geostrophic wind. The shift from dominance

of baroclinic pressure to vertical mixing effect forcing in Eq. (26) occurs at a background geostrophic wind around $U_g = 1$, roughly consistent with the shift from spindown to gravity wave regime.

The background shear and $E^{(1)}$ profile obtained with $d(\ln\gamma)/d\delta > 0$ (Fig. 1) produce a stability induced vertical flux of horizontal momentum that is zero at the surface and inversion height and has a midlevel extremum. For unstable (stable) $\delta^{(1)}$, this increases (reduces) the flux of large background momentum from aloft to the near surface. Consistent with O'Neill et al. (2010b), the resulting turbulent momentum flux divergence for background winds passing from cold to warm SST ($\delta > 0$) accelerates the surface winds in the direction of the backgrounds and induces an anticyclonic turning, while winds aloft close to the inversion experience a deceleration and cyclonic turning (Fig. 2). The vertical integral of this mixing-induced acceleration is zero, since we chose $E^{(1)} = 0$ at the sea surface.

c. *Frontally induced circulation*

The responses of the linear model vis-à-vis the observed characteristics of frontal air–sea interaction are explored using a specific example of an undulating SST front that resembles a widely cited schematic (e.g., Chelton et al. 2004; Fig. S6):

$$T^{(1)} = 0.1 \tanh\left[\frac{y - \delta y \cos(2\pi x/B)}{\Delta}\right], \qquad (29)$$

with amplitude 0.1, frontal width Δ, excursion δy in y direction, and frontal wavelength B in x (see Table 1). The coordinate system (x, y) is aligned with unit vectors $\hat{\mathbf{e}}_g$ and $\hat{\mathbf{e}}_3 \times \hat{\mathbf{e}}_g$ so that large-scale geostrophic winds blow toward positive x. The domain is a doubly periodic square with side lengths of 50 Rossby radii. This SST prototype exemplifies all physical regimes—large δy and small B yield high-curvature fronts relevant for comparison with observations of Gulf Stream and Southern Ocean rings, and their atmospheric response (Park et al. 2006; Frenger et al. 2013).

We focus on the observed characteristics of wind speed and direction, of wind stress divergence and curl, and of the coupling coefficients, all in relation to SST and its gradients. For observations, frontal impacts are separated from large scales by application of a filter that retains scales smaller than 10° latitude and 20° longitude only (Chelton et al. 2004; Chelton and Xie 2010). In our model, large-scale variability is reduced to a prescribed geostrophic wind $\mathbf{U}_g$ and the background Ekman spiral $\mathbf{u}^{(0)}$, and the largest scales are associated with the wavelength B of the SST front (Table 1). The downwind and crosswind components of the SST gradient are determined relative to the large-scale winds in observations (O'Neill et al. 2010a) and relative to surface background winds $\mathbf{u}^{(0)}|_{s_0}$ in the model.

Impacts of the background winds are explored with U_g of 0.5 and 2.0, corresponding to vertical averages of the background wind speeds (Fig. 2) of 0.36 and 1.5. In the former case, background winds are slower than the gravity wave speed and lead to an evanescent spindown, while the faster speed in the latter case leads to an oscillatory gravity wave regime. For the SST front of Eq. (29) and reference parameters (Table 1), background winds $\mathbf{u}^{(0)}$ blow along and cross the front in segments long compared to the wake and Rossby radius and thus cover a variety of length scales relative to the thermal wake and to the Rossby radius of deformation. These include the cross-frontal cases of Spall (2007) and Kilpatrick et al. (2014) with a strong downstream wake of perturbed boundary layer stability and the alongfrontal cases of Feliks et al. (2004), when boundary layer temperature has achieved thermal equilibrium and the pressure gradient forcing dominates. We refer to the frontal segments at $x = 10$ (Fig. 3a) where background winds cross at a near-right angle as "cross front" and segments where the background winds are approximately parallel to the front as "alongfront" [centered at $x = -10$ (Fig. 3a)]. The regions around the cusps of the SST front at $x = 0$ and $x = \pm 25$ afford a view of the response when winds cross the front at increasing angles and the associated increases of the cross-frontal advection. To distinguish these regimes from the type of forcing, we show the responses to the total and individual components of the forcing $\mathbf{F}$ in Eq. (21).

1) WIND SPEED AND DIRECTION

The model (Fig. 3) captures the observed covariations of spatial high-pass-filtered SST and surface wind speeds (Chelton et al. 2004; Xie 2004; Chelton and Xie 2010; Small et al. 2008) and of the wind direction (O'Neill et al. 2010a). As in observations (Chelton and Xie 2010; O'Neill et al. 2010a), frontally induced responses of wind speed $\mu^{(1)}$ and direction $\vartheta^{(1)}$ are estimated from the difference of the total (sum of background and frontally induced) surface winds and background winds. Linearizing about the background state, the speed and direction responses are determined by the frontally induced wind components aligned and across the unit vector $\hat{\mathbf{e}}_u = |\mathbf{u}^{(0)}|^{-1}\mathbf{u}^{(0)}|_{s_0}$ of the surface background wind:

$$\mu^{(1)} = \hat{\mathbf{e}}_u \cdot \mathbf{u}^{(1)} + O(\varepsilon^2) \quad \text{and} \qquad (30)$$

$$\vartheta^{(1)}|\mathbf{u}^{(0)}| = [\hat{\mathbf{e}}_u \times \mathbf{u}^{(1)}] \cdot \hat{\mathbf{e}}_3 + O(\varepsilon^2). \qquad (31)$$

The direction of the frontally induced surface winds is anticlockwise for positive values of $[\hat{\mathbf{e}}_u \times \mathbf{u}^{(1)}] \cdot \hat{\mathbf{e}}_3$.

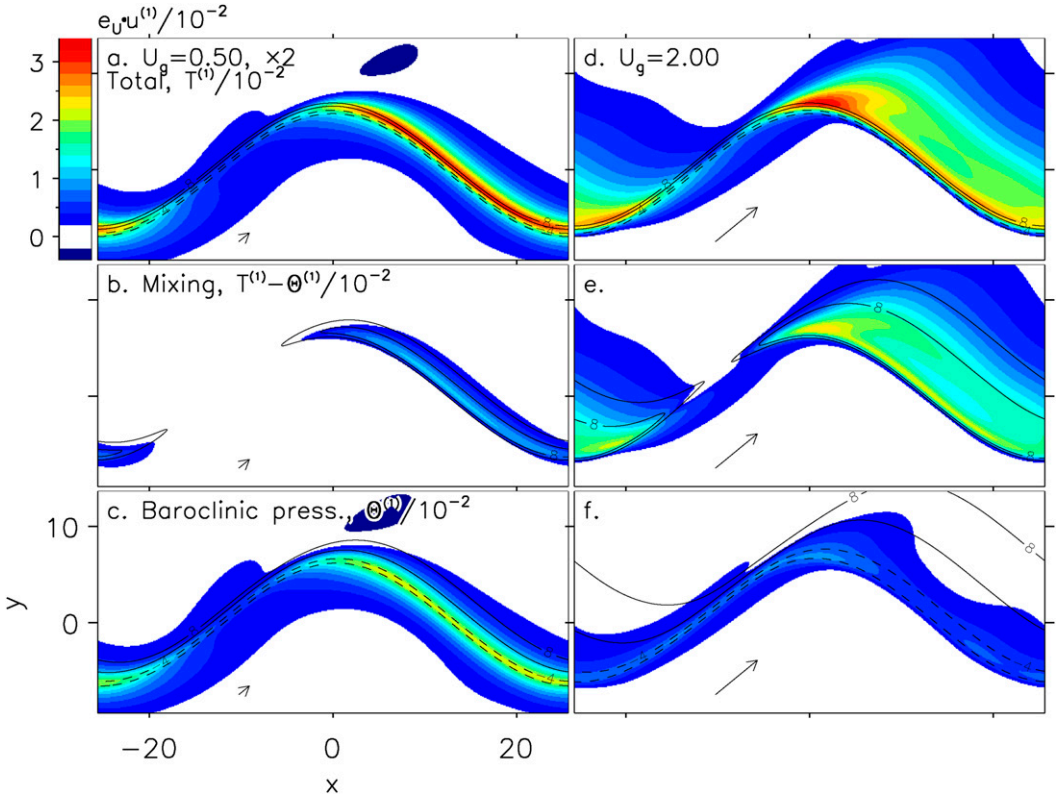

FIG. 3. Surface wind speed $\hat{\mathbf{e}}_u \cdot \mathbf{u}^{(1)}$ (color, in 10^{-2}) in response to geostrophic winds of strength (a)–(c) $U_g = 0.5$ and (d)–(f) $U_g = 2$ passing over an undulating SST front (contours). For optimal use of the dynamic range of the color bar, wind speed values in (a)–(c) have been multiplied by a factor of 2, as indicated by "×2" in (a). Shown are the responses to the (a),(d) combination of individual forcing by the (b),(e) mixing effect and (c),(f) baroclinic pressure gradient. The arrows mark the vertically averaged background winds (the blue arrow of Fig. 2) multiplied by the thermal damping time γ_Θ^{-1} so that its length depicts the scale of the thermal wake downwind of the SST front. Overplotted as lines are (a),(d) $T^{(1)}$; (b),(e) air–sea temperature difference $T^{(1)} - \Theta^{(1)}$; and (c),(f) the air temperature $\Theta^{(1)}$ (units of 10^{-2}; with contour intervals of 4 and 0 contour omitted).

For $U_g = 0.5$, wind speeds increase downstream of the cross-frontal segment (Fig. 3a). In the along-frontal segment, the speed response is weak and extends to both sides of the front. The upwind extension indicates the action of the back pressure, as forcing **F** only acts at and downstream of the SST front. The in-phase relationship between high SST and wind speed is more pronounced for stronger background winds and shows a downstream oscillatory wake associated with a damped, lee gravity wave for Froude numbers greater than one (Fig. 3d). The transition between the alongfront evanescent response to the cross-front gravity wave is seen at the cusp of the front: as the cross-frontal component of the background wind increases, the downwind wake grows, while the upwind expression diminishes, until the latter vanishes and the former exhibits an oscillation.

As expected from the scaling Eq. (26), the importance of the vertical mixing effect increases with U_g. For $U_g = 0.5$, the response of air–sea temperature difference is restricted to a narrow band in the cross-frontal segment (Fig. 3b). The baroclinic pressure forcing thus dominates the speed response in the cross-frontal segment where the baroclinic pressure gradient is aligned with the background winds (Fig. 3c). For $U_g = 2$, temperature gradients are small (Fig. 3f), and a large wake of elevated air–sea temperature differences (Fig. 3e) and concomitant vertical mixing–induced accelerations (O'Neill et al. 2010b) determine the total response.

The direction of frontally induced surface winds (Fig. 4) reflects the strong impact of the baroclinic pressure forcing for the spindown and inertial turning for the gravity wave regime. In the alongfront segment, winds over the front turn counterclockwise, consistent with a sea breeze from the cold to the warm side of the front. In the cross-front segment, winds turn in a clockwise direction (anticyclonic), because of a geostrophic response to the across-front pressure gradient. The directional modulation because of the vertical mixing effect alone

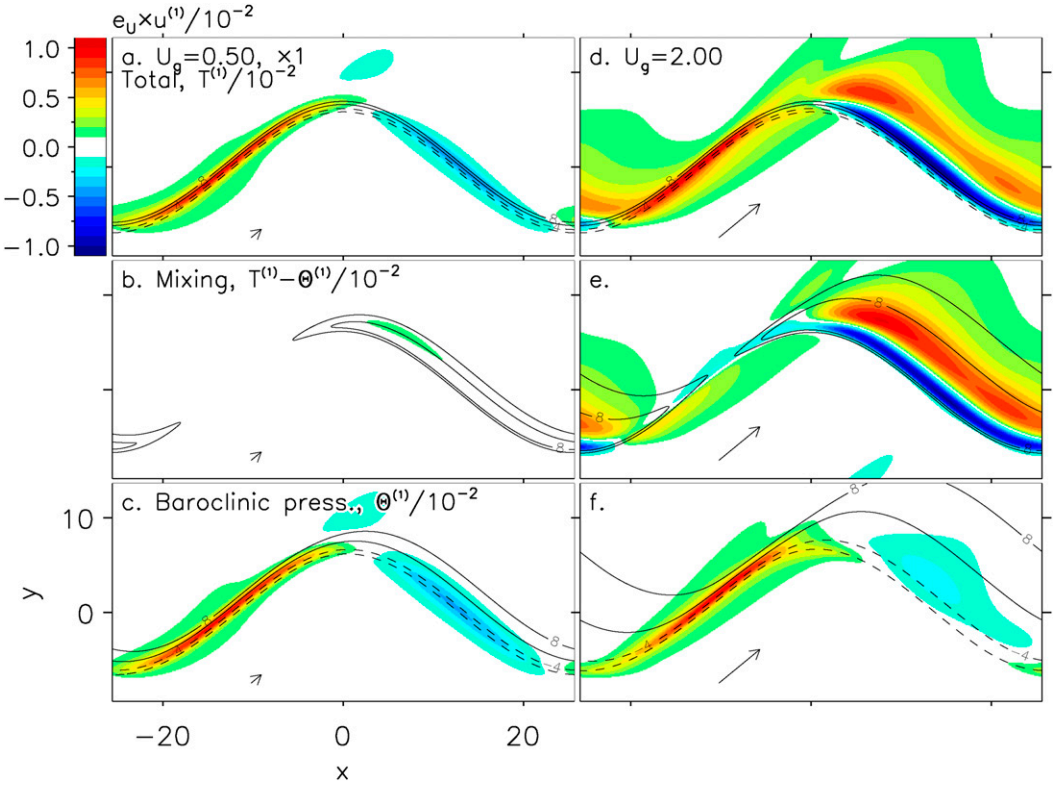

FIG. 4. As in Fig. 3, but for surface wind direction as measured by $[\hat{\mathbf{e}}_u \times \mathbf{u}^{(1)}] \cdot \hat{\mathbf{e}}_3$ (color), and values in (a)–(c) have been multiplied by a factor of 1 [i.e., the dynamic range of (a)–(c) is the same as that of (d)–(f)].

(Fig. 4b) leads to a weak anticlockwise response, associated with the development of a back-pressure gradient. For the strong wind case with $U_g = 2$, the gravity wave response includes anticyclonic turning of the winds of an inertial wave excited by the vertical mixing effect (Spall 2007; O'Neill et al. 2010b; Kilpatrick et al. 2014). The pressure forcing is small in the crosswind sector. The $U_g = 0.5$ and along-wind response are consistent with the observations reported by O'Neill et al. (2010a) in the South Atlantic and Gulf Stream. The along-frontal winds in the South Atlantic turn cyclonically toward warmer waters, while the cross-frontal winds passing from cold to warm over the Malvinas Current and Gulf Stream show an anticyclonic rotation.

2) WIND STRESS CURL AND DIVERGENCE

The model reproduces the observed characteristics of the frontally induced wind stress divergence and curl. In the cross-front segment, the wind stress divergence displays a dipole with large, positive values aligned with a downwind gradient of SST for the slow and fast background wind cases (Figs. 5, 6). Downstream, the wind stress divergence turns negative for $U_g = 0.5$ and oscillatory for $U_g = 2$. These changes are largely a result of downwind change of the wind speed (Fig. 3) and are dominated by the baroclinic pressure forcing for $U_g = 0.5$ and by the vertical mixing effect for $U_g = 2$. In the alongfront segment, the wind stress divergence forms a dipole centered on the front in response to the turning of the wind (Fig. 4). Since, in this segment, the cross-front advection by the background winds is small, both $U_g = 0.5$ and $U_g = 2$ show an evanescent response expected from spindown. Air and ocean temperatures are in equilibrium, so the wind stress divergence is a response to the baroclinic pressure forcing only.

The wind stress curl (Figs. 7, 8) is more complicated than the strong curl in the alongfront segment suggested by qualitative reasoning based on the vertical mixing effect (Businger and Shaw 1984; Chelton et al. 2004). In the cross-front segment, the wind stress curl forms a dipole, with negative values upstream and positive values downstream of the front. In the alongfront segment, the curl vanishes at the SST front and reaches largest negative values on the cold and largest positive values on the warm side of the front toward the cusps of the front, when the air–sea temperature difference is no longer in equilibrium and advection comes into play. Negative wind stress curl is collocated with a positive crosswind SST

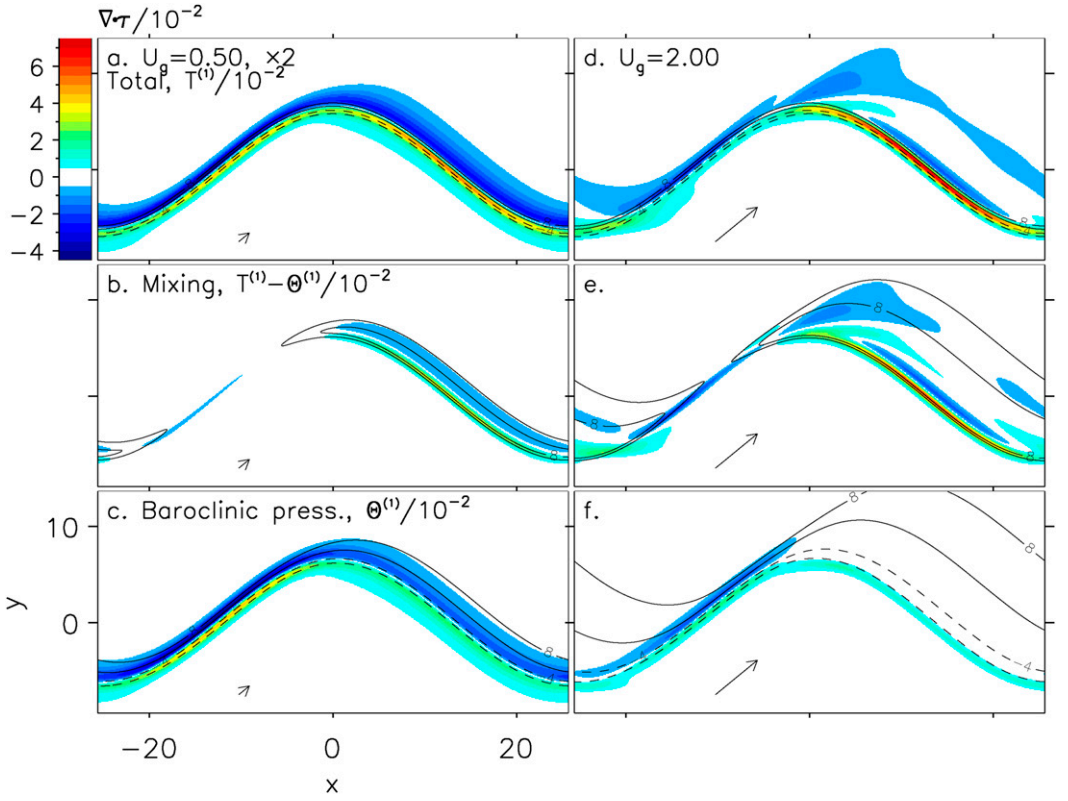

FIG. 5. As in Fig. 3, but for wind stress divergence (color). For ease of comparison, wind stress divergence values in (a)–(c) have been multiplied by a factor of 2.

gradient (Fig. 8), as expected from observations. This relationship stems from the vertical mixing term (Figs. 8b,e), while the pressure gradient produces a wind stress curl that is out of phase with the crosswind SST gradient. Since the vertical mixing term is dominant for the strong background wind case, the total response is collocated with the crosswind SST gradient for $U_g = 2$.

In observations, frontally induced surface wind speed and direction are phase shifted with respect to the angle of SST gradient and background winds, so the wind stress divergence is enhanced, but the wind stress curl is reduced (O'Neill et al. 2010a). The model reproduces this finding. Use of the surface wind component Eqs. (30) and (31) yields the linearized formulation of the surface stress divergences in terms of downwind changes of the speed and crosswind changes of the direction, as well as of the curl in terms of crosswind changes of speed and downwind changes of direction (e.g., O'Neill et al. 2010a). Considering the cusp of the front at $-5 \le x \le 5$ for $U_g = 0.5$, the surface wind speed increases as the background winds cross the front toward warm SST (Fig. 3), while the wind direction is positive (Fig. 4). This implies that surface stress divergence due to downwind speed and the crosswind direction gradients have the same sign. On the other hand, the crosswind speed gradients lead to negative, but the downwind direction gradients lead to positive wind stress curl.

5. Coupling coefficients

The coupling coefficients α_D between wind stress divergence and downwind SST gradients and α_C between wind stress curl and crosswind SST gradients

$$\nabla \cdot \boldsymbol{\tau}^{(1)} = \alpha_D[\hat{\mathbf{e}}_u \cdot \nabla T^{(1)}] + \text{residual} \quad \text{and}$$
$$[\nabla \times \boldsymbol{\tau}^{(1)}] \cdot \hat{\mathbf{e}}_3 = \alpha_C[\hat{\mathbf{e}}_u \times \nabla T^{(1)}] \cdot \hat{\mathbf{e}}_3 + \text{residual} \qquad (32)$$

are determined by a least squares fit from the model solution for the undulating SST front. The coefficients are strong functions of the background winds and forcing process (Table 2), but α_D is consistently larger than α_C, as found in observations and general circulation models (Song et al. 2009; Chelton and Xie 2010; Bryan et al. 2010). For $U_g = 0.5$, α_D is 7.9×10^{-2} and increases to 2.4×10^{-1} for $U_g = 2$ (Figs. 6a,d). The dominant forcing of this coupling coefficient is the vertical mixing effect for both $U_g = 0.5$ and $U_g = 2$. This is because of the higher correlation between the fields, even though the wind stress

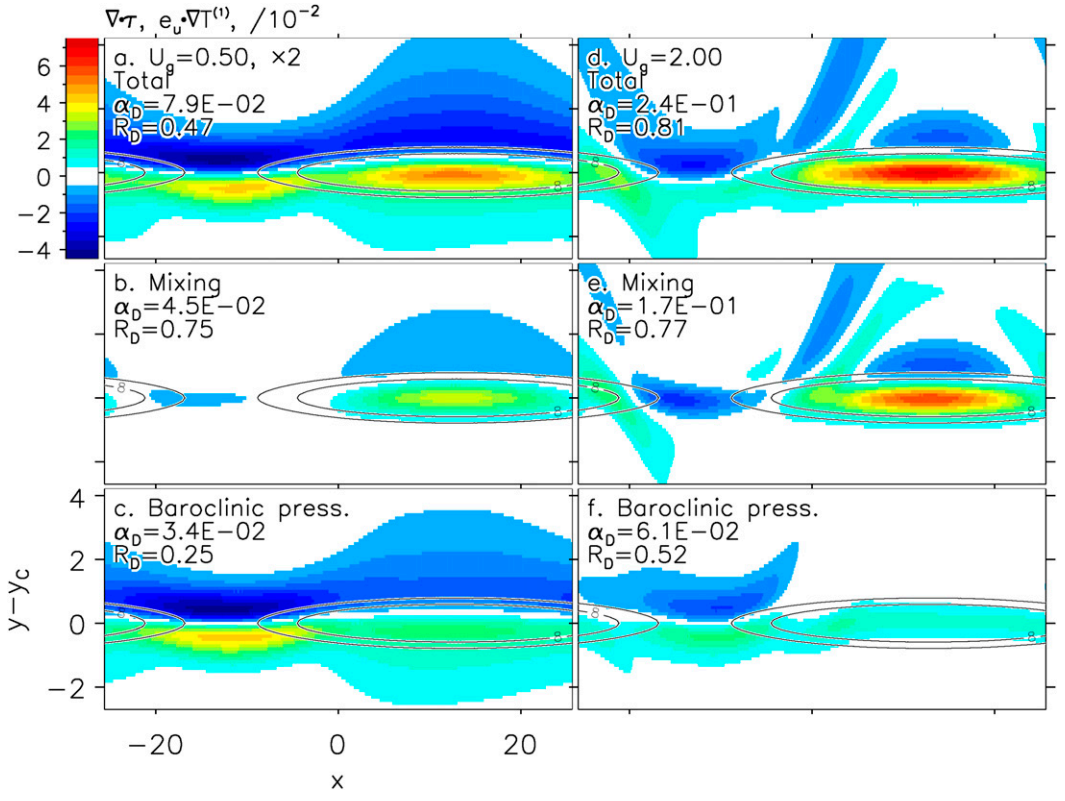

FIG. 6. As in Fig. 5, but for wind stress divergence (color) and downwind gradient of SST (contour, units of 10^{-2}). To focus on the details around the SST front, the ordinate is the distance in y from the center of the SST front. The coupling and correlation coefficients, α_D and R_D, respectively, between the downwind SST gradient and the wind stress divergence are indicated in the upper-left corner of each panel.

divergence variance is small for $U_g = 0.5$ (Figs. 5b,c,e,f). For $U_g = 0.5$, α_C is practically zero because of an out-of-phase relation between curl and crosswind SST gradient and the smaller variance of wind stress curl compared to divergence (Figs. 6, 8). For $U_g = 2$, the correlation underlying α_C hovers around -0.35 as a result of the prominence of the vertical mixing effect, but the variance of wind stress curl remains smaller than that of the wind divergence (Figs. 8d–f).

Since the dominance of α_D over α_C is seen in response to the individual forcing by the vertical mixing effect and baroclinic pressure forcing (Figs. 6, 8), it is governed by the distinct dynamics of the wind stress divergence and wind stress curl, rather than by peculiarities of the forcing. The explanation of the coupling coefficients therefore hinges on the relationship between coupling coefficients and the transfer functions $\tilde{\mathbf{R}}$ of Eq. (25).

Fourier transforming the Eq. (32) in the horizontal wavenumber space

$$\widetilde{\nabla \cdot \boldsymbol{\tau}^{(1)}} = \imath\alpha_D(\hat{\mathbf{e}}_u \cdot \mathbf{k})\tilde{T} + \text{residual} \quad \text{and}$$
$$\widetilde{[\nabla \times \boldsymbol{\tau}^{(1)}] \cdot \hat{\mathbf{e}}_3} = \imath\alpha_C(\hat{\mathbf{e}}_u \times \mathbf{k}) \cdot \hat{\mathbf{e}}_3\tilde{T} + \text{residual} \qquad (33)$$

shows that α_D and α_C correspond to slopes in along- and cross-background wind directions, $\hat{\mathbf{e}}_u$ and $\hat{\mathbf{e}}_3 \times \hat{\mathbf{e}}_u$, of linear planes that are fit to the imaginary parts of the wind stress divergence and curl transfer functions $\tilde{\mathbf{R}}_{\nabla\cdot\boldsymbol{\tau}}$ and $\tilde{\mathbf{R}}_{\nabla\times\boldsymbol{\tau}}$.

For $U_g = 0.5$, the imaginary part of the wind stress divergence transfer function $\tilde{\mathbf{R}}_{\nabla\cdot\boldsymbol{\tau}}$ increases approximately linearly with $\hat{\mathbf{e}}_u \cdot \mathbf{k}$, and the real part is small (Figs. 9a,c). The real part dominates in the sector aligned with $(\hat{\mathbf{e}}_u \times \mathbf{k}) \cdot \hat{\mathbf{e}}_3$ and shows an approximate parabolic increase. This is the spectral representation of the 90° phase shift between the wind stress divergence and SST front found in the along-wind segment of the undulating front (Fig. 5). The inertial, anticyclonic turning of the surface winds of the undulating front case are reflected in the transfer function being slightly larger for negative than for positive values of $(\hat{\mathbf{e}}_u \times \mathbf{k}) \cdot \hat{\mathbf{e}}_3$, while the sign of the downwind wavenumber remains unchanged. This asymmetry is further amplified for the $U_g = 2$ gravity wave solution with large real parts in the downwind wavenumber sector (Figs. 10a,c).

For $U_g = 0.5$, the imaginary part of the wind stress curl transfer function (Fig. 9d) shows the near-linear dependence on the crosswind wavenumber, punctuated by

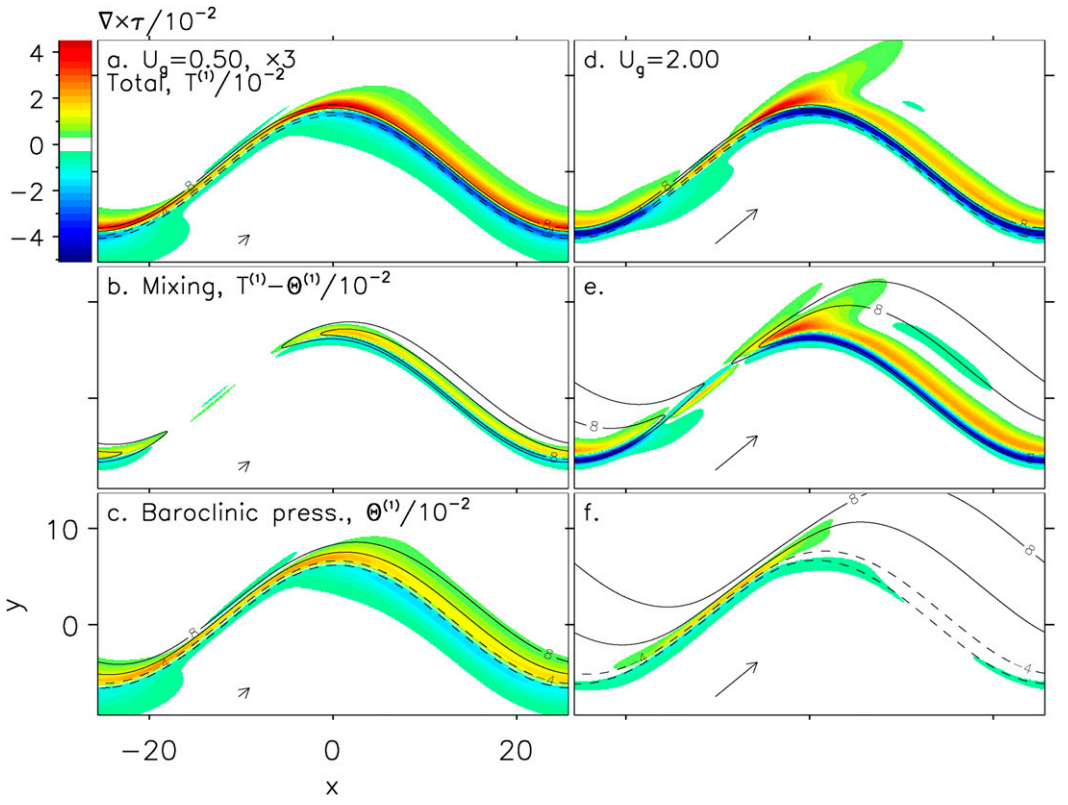

FIG. 7. As in Fig. 5, but for wind stress curl (color). For ease of comparison, wind stress curl values in (a)–(c) have been multiplied by a factor of 3.

values of opposite sign for small downwind wavenumbers. It is this wedge that reduces the coupling coefficient of the wind stress curl compared to that of the wind stress divergence and leads to the largest curl when the winds cross a front at oblique angles, rather than in the alongfront segment (Fig. 7). The real part of the response (Fig. 9b) is large in the crosswind sector but vanishes for the zero downwind wavenumbers. For $U_g = 2$, the response pattern remains, albeit with larger slope, but the wedge of oppositely signed values is narrower. The wind stress curl coupling coefficient is therefore closer to that of the wind stress divergence.

To diagnose the processes that determine the wind stress curl and divergence transfer functions, and thereby the coupling coefficients, we consider the vertical averages, $\int_0^1 ds'$ denoted by an overbar, of the potential vorticity and the divergence equations. The horizontal divergence of the momentum equation [Eq. (20)] and continuity equation [Eq. (22)] yield

$$\underbrace{-\overline{\mathbf{u}^{(0)}\cdot\nabla[\nabla\cdot\mathbf{u}^{(1)}]}}_{\text{Advection}}\ \underbrace{-\overline{\nabla w^{\star(1)}\cdot\partial_s\mathbf{u}^{(0)}}}_{\text{Tilt}}+\underbrace{\overline{\hat{\mathbf{e}}_3\cdot[\nabla\times\mathbf{u}^{(1)}]}-\nabla^2h^{(1)}+\frac{1}{2}\nabla^2\Theta^{(1)}}_{\text{Ageostrophic relative vorticity}}=\nabla\cdot\boldsymbol{\tau}^{(1)}|_{s=0}. \tag{34}$$

In the nonadvective limit, the wind stress divergence balances the ageostrophic residual between the vertical averages of the relative vorticity $\hat{\mathbf{e}}_3\cdot[\nabla\times\mathbf{u}^{(1)}]$ and of geostrophic relative vorticity $\nabla^2h^{(1)}-(1/2)\nabla^2\Theta^{(1)}$.

The curl of the vertical averaged momentum balance equation [Eq. (20)] and the continuity equation [Eq. (22)] yield the conservation of potential vorticity:

$$-\overline{\mathbf{u}^{(0)}\cdot\nabla\{[\nabla\times\mathbf{u}^{(1)}]\cdot\hat{\mathbf{e}}_3-h^{(1)}\}}-\hat{\mathbf{e}}_3\cdot\overline{\nabla w^{\star(1)}\times\partial_s\mathbf{u}^{(0)}}=\hat{\mathbf{e}}_3\cdot\nabla\times\boldsymbol{\tau}^{(1)}|_{s=0}. \tag{35}$$

The potential vorticity budget balances the advection of potential vorticity $[\nabla\times\mathbf{u}^{(1)}]\cdot\hat{\mathbf{e}}_3-h^{(1)}$ by the background winds, the generation of potential vorticity by tilting of the

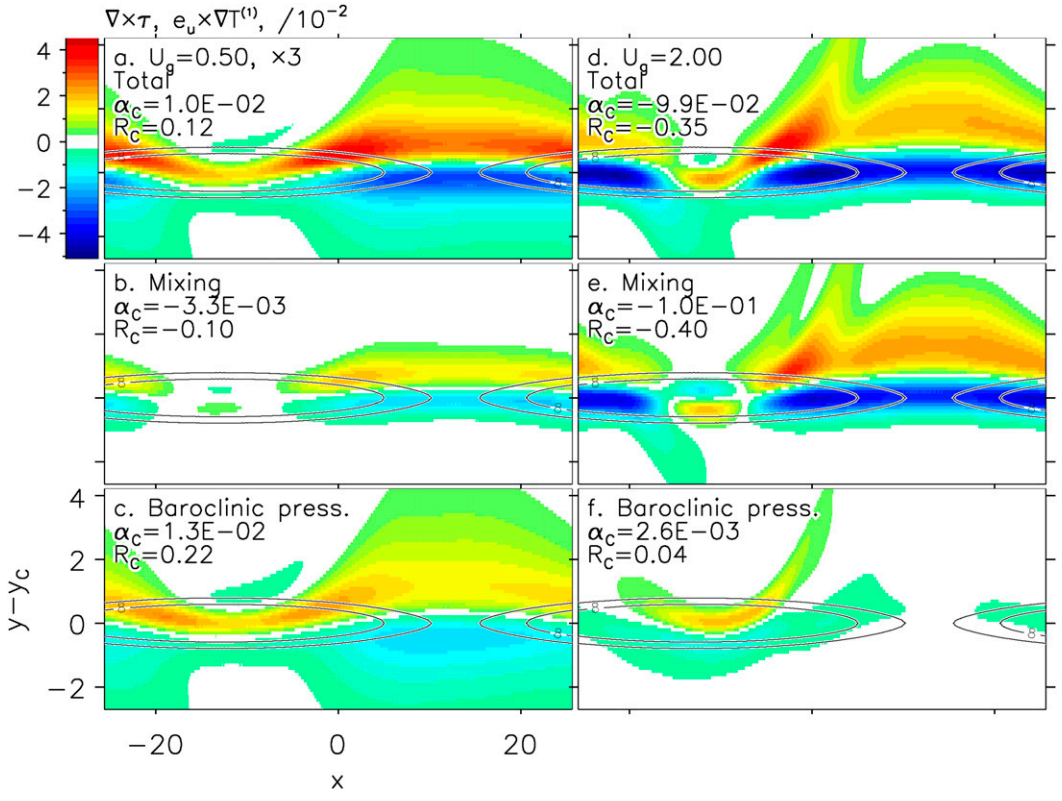

FIG. 8. As in Fig. 6, but for wind stress curl (color), crosswind gradient of SST (contour), and α_D and R_C indicated in the upper-left corner of each panel.

background shear, and the curl of the total surface stress. The budget equation [Eq. (35)] recovers the classical spindown and its application to SST fronts. In the nonadvective $\mathbf{u}^{(0)} = 0$ limit, the total surface wind stress curl is nil. This is achieved by the secondary circulation because of the divergence of the Ekman transports that displace the inversion height until the wind stress curl shuts down. In the classical Ekman formulation with small Ekman number of the geostrophic wind, this implies that the surface baroclinic pressure gradient in $\mathbf{F}$ in Eq. (21) is cancelled by the barotropic back-pressure gradient so that the surface geostrophic winds and surface stress vanish. For a strong baroclinic pressure gradient in $\mathbf{F}$, this balance is modified by the surface stress because of the geostrophic and ageostrophic shears (Cronin and Kessler 2009), but it again adjusts the back pressure to render the total wind stress curl zero. Since the back pressure directly affects only the horizontal transports, the hallmark of spindown is that the curl of the frontally induced wind stress [Eq. (24) with our choice of $E^{(1)} = 0$ at $s = 0$] is a residual of offsetting contributions:

$$\nabla \times \boldsymbol{\tau}^{(1)}|_{s=0} = \frac{E^{(0)}}{s_0} \nabla \times \left\{ \underbrace{\overline{\mathbf{u}^{(1)}}}_{\text{Transport}} + \underbrace{[\mathbf{u}^{(1)}|_{s_0} - \overline{\mathbf{u}^{(1)}}]}_{\text{Shear}} \right\} \quad (36)$$

because of near-surface winds associated with frontally induced layer transport and shear. According to Eq. (34), the associated surface wind stress divergence is nonzero, since in the frictional boundary layer, an exact geostrophic transport, with vanishing frontally induced ageostrophic relative vorticity, cannot be achieved. The nonrotating limit yields zero geostrophic relative vorticity and implies a thermally direct, frictional balance of the pressure gradient, with the cross-frontal surface stress akin to a sea breeze.

Transforming Eqs. (34) and (35) to wavenumber space yields the budgets governing the transfer functions $\tilde{\mathbf{R}}_{\nabla\cdot\boldsymbol{\tau}}$ and $\tilde{\mathbf{R}}_{\nabla\times\boldsymbol{\tau}}$. For $U_g = 0.5$, $\tilde{\mathbf{R}}_{\nabla\cdot\boldsymbol{\tau}}$ is dominated by the vertical mixing effect (Fig. 11) that primarily affects the imaginary part of stress divergence due to surface shear in Eq. (36) and is responsible for the fit with the coupling coefficient. The stress divergence is balanced by the ageostrophic relative vorticity and partially offset by advection and tilt for the real part of the transfer function. The impact of the baroclinic pressure forcing (Fig. 12) is largest in the crosswind wavenumber sector, as expected from the imprint of SST gradients on the hydrostatic pressure gradient when the winds blow along an SST front. Here, the real part of the transfer function is on par with the

TABLE 2. Coupling coefficients times 100 between wind stress divergence and downwind gradient of SST α_D, between wind stress curl and crosswind gradient of SST α_C, and their ratio α_C/α_D as a function of nondimensional eastward geostrophic winds (Froude number) U_g. Parameters for the reference case are listed in Table 1; in subsequent columns, the vertical mixing effect is isolated, and the coefficient E_0 and γ are doubled, while the remaining parameters remain at their reference values. Results are shown for the undulating front of Eq. (29), the reference case, a broad and a short wavelength, and strongly undulating fronts.

	Reference		$\nabla\Theta = 0$		$E_0 = 1$		$\gamma = 0.6$	
U_g	0.5	2	0.5	2	0.5	2	0.5	2
Undulating front (see Table 1)								
α_D	8	24	5	17	12	19	3	10
α_C	1	−10	0	−10	1	−3	0	−5
α_C/α_D	0.13	−0.42	−0.07	−0.58	0.10	−0.18	0.09	−0.49
Broad front ($\Delta = 2.5$)								
α_D	2	18	1	15	2	13	0	7
α_C	1	−3	0	−2	1	−3	0	−3
α_C/α_D	0.33	−0.19	0.32	−0.16	0.32	−0.22	1.07	−0.40
Rapid and large frontal undulations ($B = 2$ and $\delta y = 2$)								
α_D	16	40	10	33	26	35	5	12
α_C	−3	−16	−5	−17	−4	−41	0	−5
α_C/α_D	−0.22	−0.40	−0.47	−0.51	−0.15	−1.2	0	−0.40

imaginary contribution. Again, the shear-induced stress balances the ageostrophic relative vorticity, with some offset by advection and tilt. For stronger background wind $U_g = 2$, the wind stress divergence reduces to a small contribution to the main balance between ageostrophic vorticity and advection (not shown).

For $U_g = 0.5$, the potential vorticity budget shows in the crosswind sector the near cancellation of the curl contributions by the shear and transport. This is the hallmark of geostrophic spindown, and it occurs both in response to the vertical mixing effect (Figs. 13) and to baroclinic pressure gradients (Fig. 14). For both forcings, the small residual, net wind stress curl is balanced by potential vorticity advection and generation by vortex tilting. Forcing by the vertical mixing effect is the key to the coupling coefficient of the wind stress curl, while the baroclinic pressure gradient forcing is strongest in the cross-front wavenumber sector (that corresponds to winds blowing along the SST front). For stronger background winds, $U_g = 2$, the cancellation of the wind stress curls associated with shear and transports remains but it is limited to a narrower, crosswind wavenumber sector (not shown).

The importance of spindown is limited to the crosswind sector, marked by wavenumbers with magnitude k_{spin} for which advection and wind stress curl in Eq. (35) balance

$$\cos(\phi)\frac{|\mathbf{u}^{(0)}|}{\sqrt{E}}\frac{1+k_{\text{spin}}^2}{k_{\text{spin}}} = 1, \tag{37}$$

where ϕ is the angle between $\mathbf{k}$ and $\mathbf{u}^{(0)}$. The relative vorticity has been scaled using geostrophy, and the vertical length scale of the surface stress $\boldsymbol{\tau}^{(1)} = E\partial_s\mathbf{u}^{(1)}$ is $\sqrt{E}$ so that the geostrophic spindown time is $|\mathbf{k}|^{-2}E^{(0)^{-1/2}}$ (Holton 1965a; Benthuysen 2010). Wavenumbers k_{spin} that satisfy Eq. (37) (indicated by dotted lines in Figs. 9, 10, 13, and 14) separate higher wavenumbers dominated by advection of potential vorticity from lower wavenumbers dominated by local spindown. The difference of wind stress curl response to SST fields of along-wind fronts and ocean eddies (Businger and Shaw 1984; Park et al. 2006; Frenger et al. 2013) is that the latter excite wavenumbers larger than k_{spin}.

6. Sensitivity and comparison with observations

The sensitivity of the coupling coefficients to the formulation of the vertical exchange coefficients and to the SST distribution are explored by doubling the background eddy coefficient amplitude E_0 and its vertical decay scale γ and by considering a broad SST front with $\Delta = 2.5$ and a rapidly fluctuating, large-amplitude front with $\delta y = 2$ and $B = 2$ (Table 2).

Coupling coefficients show a strong dependence on the background winds, the vertical mixing formulation, and, as expected from the transfer functions, the minimum SST scale (Table 2). The simulated order of nondimensional α_D is 10^{-1}, which corresponds to observed values of α_D of $10^{-2}\,\mathrm{N\,K^{-1}\,m^{-2}}$ (O'Neill et al. 2010a), using a dimensional conversion factor of $E\rho_a fH[(\Delta\Theta/\Theta_0)gH]^{0.5}\Delta\Theta^{-1} = O(10^{-1}\,\mathrm{N\,K^{-1}\,m^{-2}})$ for $f = 10^{-4}\,\mathrm{s^{-1}}$, $H = 1000\,\mathrm{m}$, an air density $\rho_a = 1\,\mathrm{kg\,m^{-3}}$, and an inversion strength $\Delta\Theta = 9\,\mathrm{K}$ (Betts 1989).

Coupling coefficients increase with background winds, including the experiment with forcing by only the vertical mixing effect. This is consistent with an increase of the vertical mixing effect following Eq. (26), the steeper slopes of the transfer functions (Figs. 9, 10),

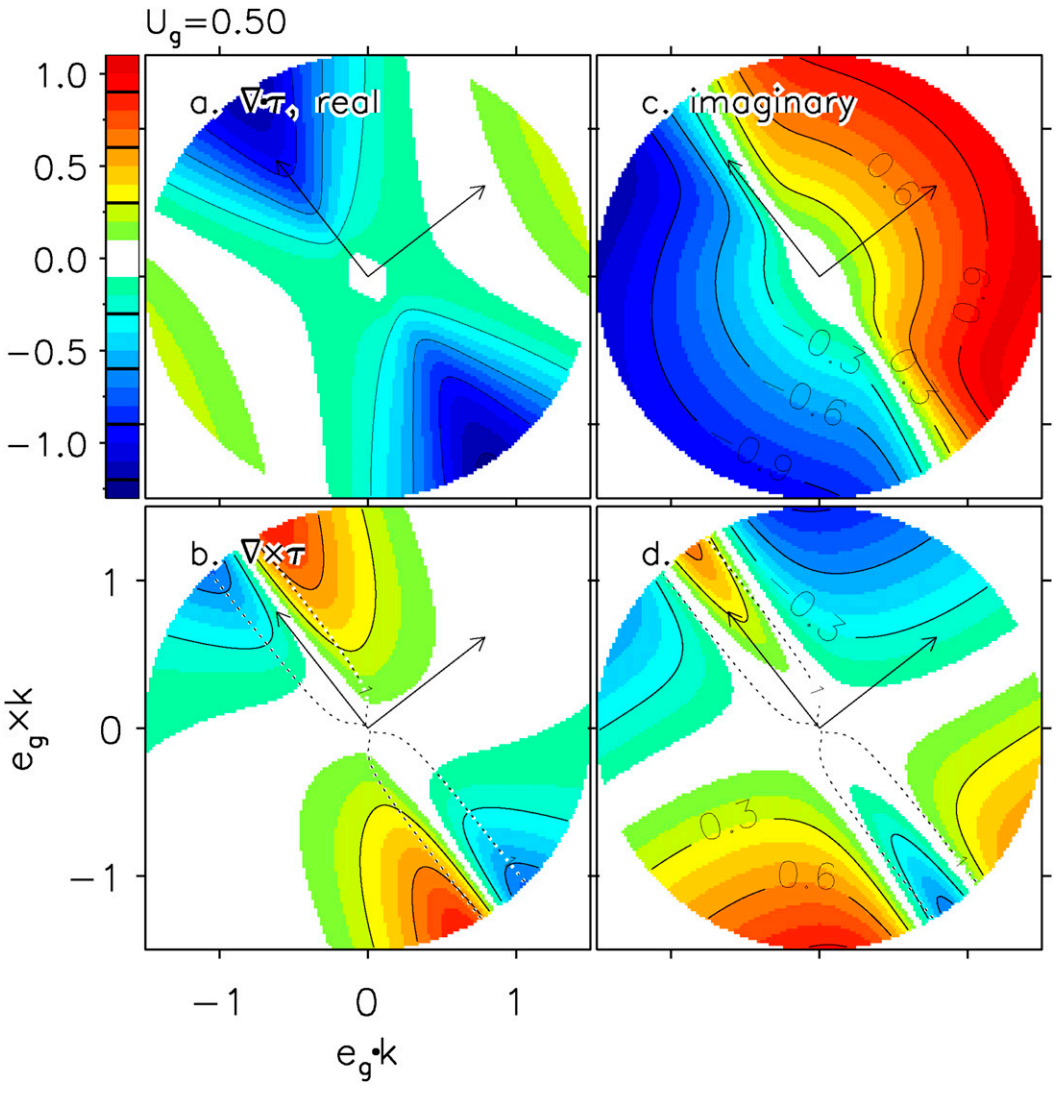

FIG. 9. Real and imaginary parts of the transfer function of the wind stress (a),(c) divergence and (b),(d) curl for $U_g = 0.5$ as a function of wavenumber components $\hat{\mathbf{e}}_g \cdot \mathbf{k}$ and $[\hat{\mathbf{e}}_g \times \mathbf{k}] \cdot \hat{\mathbf{e}}_3$, in direction of and across the large-scale geostrophic wind, respectively. Directions downwind and across the surface winds, $\hat{\mathbf{e}}_u$ and $\hat{\mathbf{e}}_3 \times \hat{\mathbf{e}}_u$, respectively, are marked by arrows, with the downwind direction pointing toward the upper right. The dotted lines in (b),(d) mark the separation of the spindown from advective regimes of potential vorticity according to Eq. (37).

the reduction of k_{spin} in Eq. (37), and the reduction of the wavenumber wedge dominated by spindown.

For all but two cases, the coupling coefficient magnitudes for wind stress divergence are larger than for the wind stress curl (Table 2). This implies the ratios α_C/α_D have magnitudes less than one, consistent with the observed values that vary regionally and seasonally between 0.4 and 0.75 (O'Neill et al. 2010a). The only exceptions occur for the smooth frontal case for $\gamma = 0.6$, where both α_D and α_c are nil and for the large amplitude, rapidly undulating front for $E_0 = 1$. In this case, coupling coefficients likely result from gravity lee-wave resonance excited by multiple crossings of the front. For strong wind and sharp frontal cases, α_C values are negative, as observed (O'Neill et al. 2010a). For weak wind cases, coupling coefficients and correlation for curl are small, consistent with the out-of-phase relationship of the SST gradient and wind stress curl expected from the transfer function in response to pressure gradient forcing (Fig. 14).

The responses to a smooth front are equivalent with a coarsening of the model resolution and yield a reduction of the coupling coefficients (Table 2). This mimics the simulation at a variety of resolutions and changes induced in the atmospheric reanalysis by the use of a higher-resolution SST (Song et al. 2009; Bryan et al.

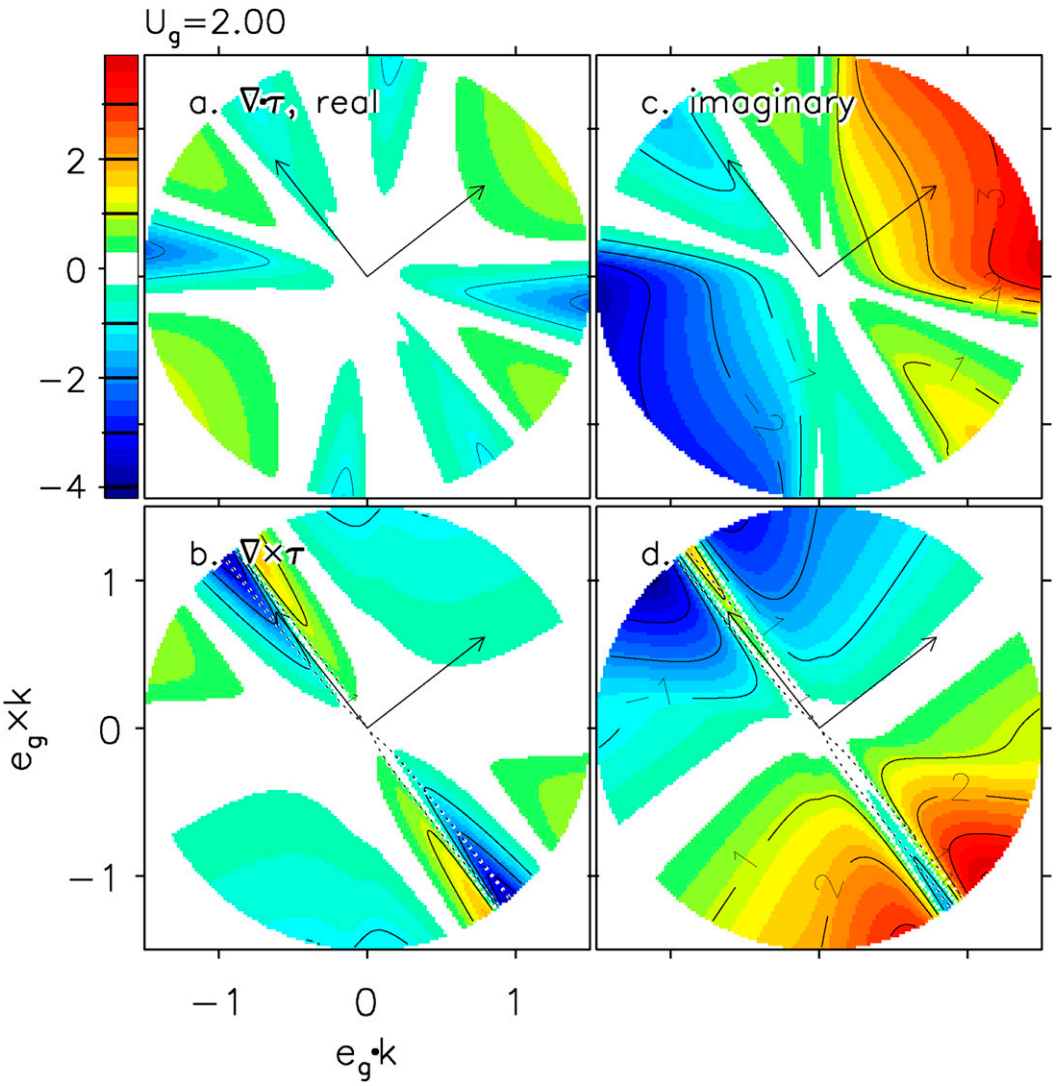

FIG. 10. As in Fig. 9, but for $U_g = 2$.

2010). A doubling of E_0 leads to inconsistent changes of the coupling coefficients as a function of the background Froude number. A doubling of the depth scale γ of the Ekman number decreases the coupling coefficients and leads to a consistent negative sign of α_C expected from observations (O'Neill et al. 2010a), while the larger stability dependence increases the importance of the forcing by the mixing effect and the coupling coefficients. The strong sensitivity of the coupling coefficient to the mixing formulation was suggested in the interpretation of the model simulations (Song et al. 2009) and suggests that observations of the coupling coefficients, the SST distribution, and the background winds may be used to constrain the vertical exchange coefficients in the atmospheric boundary layer.

7. Conclusions

Observations of the impacts of SST fronts on the atmospheric boundary layer in the extratropics show ubiquitous covariations of the wind stress divergence with the downwind SST gradient and of a negative wind stress curl with the positive crosswind SST gradient (for SST increasing to the left of the winds). The associated regressions—called coupling coefficients—are positive for the divergence and negative for the curl, and their magnitudes are systematically larger for the divergence than for the curl. We explain this observational finding by distinct dynamics of the wind stress divergence and curl. Wind stress divergence results from either large-scale winds crossing the front or from a thermally direct, cross-frontal circulation. Wind stress curl, expected to

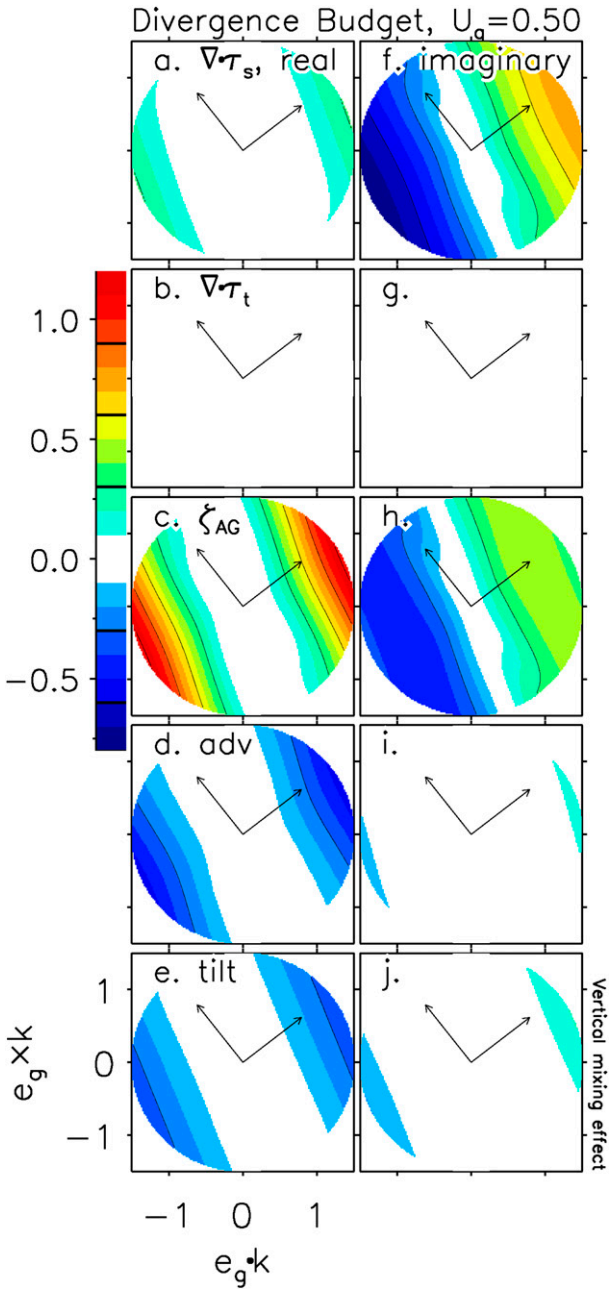

FIG. 11. Transfer function for $U_g = 0.5$ of the vertically integrated divergence budget of Eq. (34) in response to the vertical mixing effect only: (a)–(e) the real part out of phase and (f)–(j) the imaginary part in phase with the downwind SST gradient. The divergences of the surface wind stress associated with (a),(f) the layer shear and (b),(g) layer transports are balanced by (c),(h) ageostrophic relative vorticity of the transport and vertical averages of (d),(i) horizontal advection and (e),(j) the tilt term. The solid arrows mark the unit vector aligned (to upper right) and across the surface background winds.

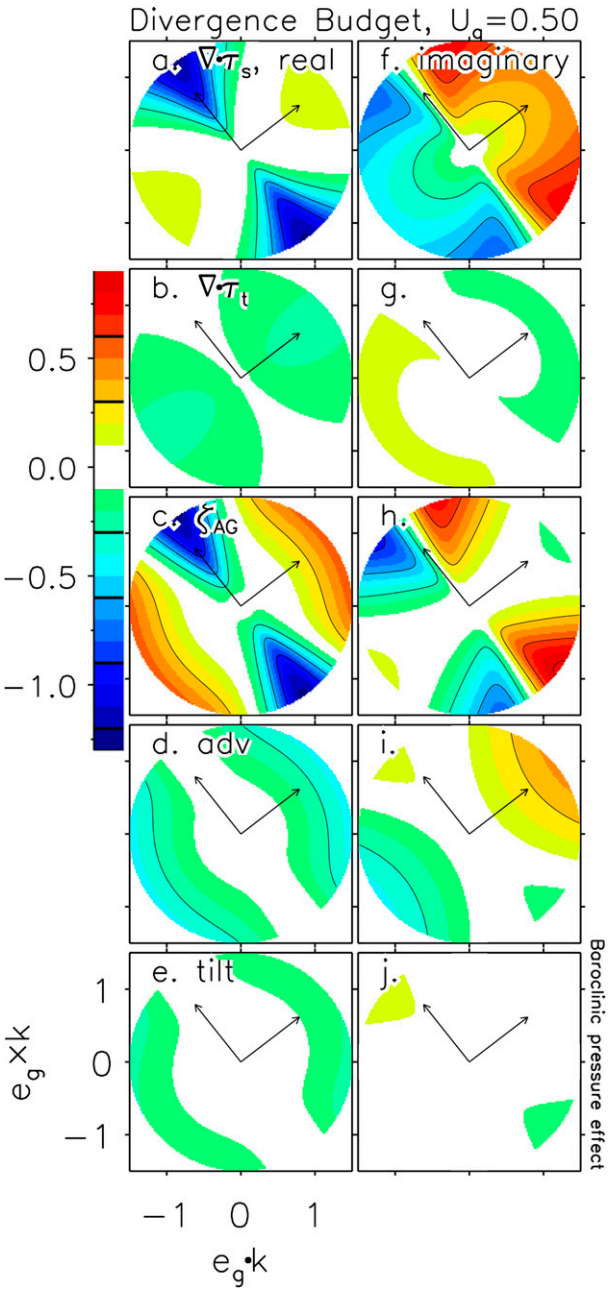

FIG. 12. As in Fig. 11, but for the divergence budget in response to the baroclinic pressure forcing only.

be largest when winds are parallel to SST fronts, is reduced through geostrophic spindown and thereby yields weaker coupling coefficients.

To show these dynamics, we introduce a shallow water model for the atmospheric boundary layer, coupled by air–sea heat fluxes to SST and bounded aloft by a strong inversion with zero turbulent and radiative fluxes. The model is forced by a prescribed, large-scale, barotropic, and time-independent geostrophic wind. Model dynamics

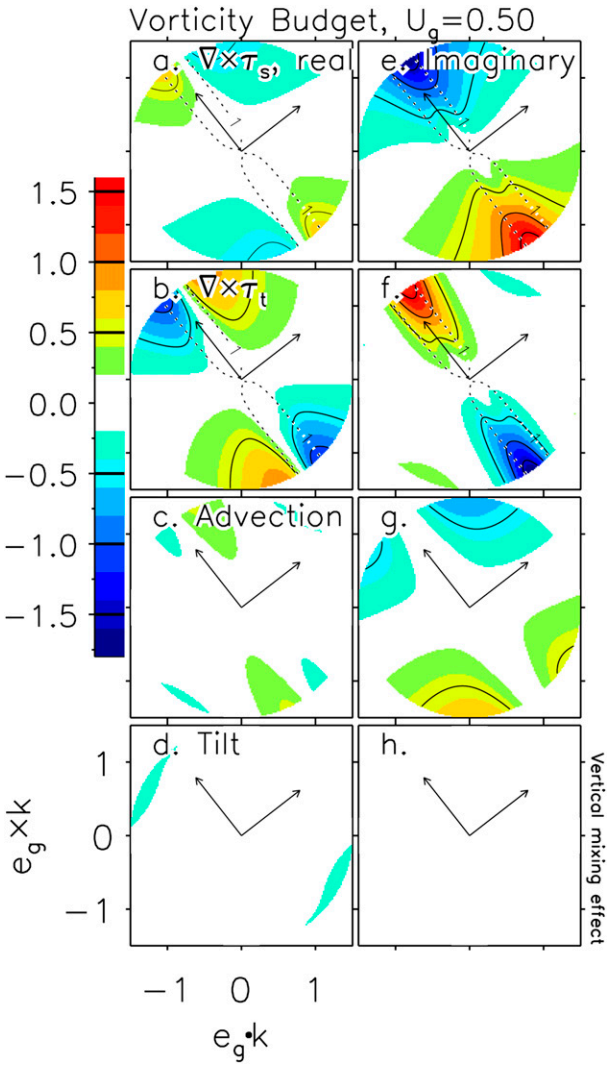

FIG. 13. Transfer function for $U_g = 0.5$ of the vertically integrated potential vorticity budget of Eq. (35) forced by the vertical mixing effect only: (a)–(d) the real part out of phase and (e)–(h) the imaginary part that is in phase with the crosswind SST gradient. The components of the wind stress curl associated with (a),(e) the layer shear and (b),(f) layer transports are balanced by the vertical averages of (c),(g) horizontal advection and (d),(h) the tilt term. The dotted lines in (a),(b),(e),(f) mark the separation of the spindown from advective regimes of potential vorticity according to Eq. (37). The solid arrows mark unit vector aligned (to upper right) and across the surface background winds.

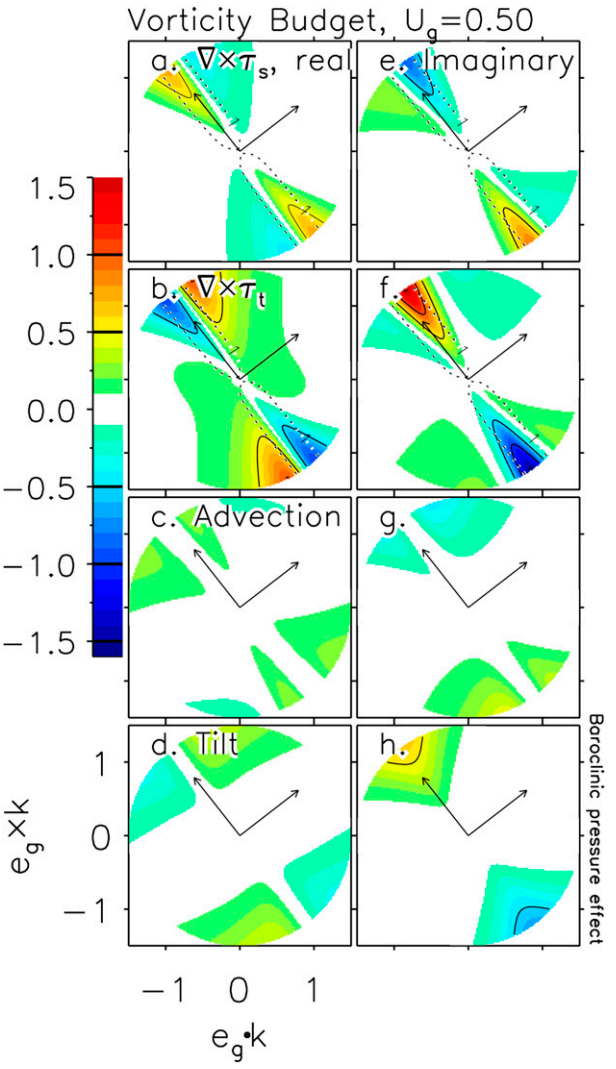

FIG. 14. As in Fig. 13, but for the potential vorticity budget in response to baroclinic pressure forcing only.

are obtained by linearization of the circulation induced by weak SST variations about a background state of an Ekman spiral and constant SST. The heat budget assumes vertically constant temperatures and balances advection by background winds and air–sea heat fluxes. For spatial scales smaller than a Rossby radius of deformation, lateral mixing parameterizes the smoothing action of a sea breeze. The resulting frontally induced temperatures are independent of frontally induced winds and force the momentum equations by baroclinic pressure gradients (Lindzen and Nigam 1987) and by the vertical mixing effect (Hayes et al. 1989; Wallace et al. 1989). The importance of the latter relative to the former forcing is given by Eq. (26) and increases with background winds and stress, with the thermal adjustment time of the boundary layer, and with the sensitivity of vertical mixing to the air–sea temperature difference.

Frontally induced winds are governed by the classical Rossby adjustment problem, albeit in the presence of vertical mixing and background advection. For cross-frontal background winds faster than the gravity wave speed (Froude numbers greater than one) the frontally induced circulation is characterized by lee gravity waves (Spall 2007; Kilpatrick et al. 2014). Froude numbers less than one yield the geostrophic regime and a dependence

of the length scale relative to k_{spin}^{-1} of Eq. (37) that corresponds to the distance traveled by cross-frontal background advection in spindown time (Greenspan and Howard 1963; Holton 1965a). For length scales larger than k_{spin}^{-1}, Ekman pumping reduces the wind stress curl to zero (Feliks et al. 2004) or to a balance with tilt production of potential vorticity. For scales smaller than k_{spin}^{-1}, the wind stress curl remains large and balances advection of potential vorticity.

The model reproduces the observed characteristics of frontal air–sea interaction: wind speeds increase (decrease) over warm (cold) waters downwind of a front; and the wind stress divergence is correlated with the downwind gradient of SST, while the regression of the wind stress curl with the crosswind gradient of SST is weaker, and negative because of the dominance of the vertical mixing mechanism. Overall, the coupling coefficients span the range of observations (O'Neill et al. 2010a) and depend on the background winds, the scales of the SST distribution, and the vertical mixing formulation. The increase of the coupling coefficients found as the SST variance includes scales close to the Rossby radius of deformation is consistent with model simulations comparing the atmospheric responses to smooth versus high-resolution SST fields (Song et al. 2009).

While our model includes all physical processes cited in the context of frontal air–sea interaction and captures the observed characteristics, it makes a number of assumptions. The model is in steady state, consistent with the observational focus on time scales long compared to synoptic atmospheric variability (Chelton and Xie 2010; O'Neill et al. 2010a) and a spindown time scale approaching an inertial period as the scales approach the Rossby radius of deformation (Holton 1965a). The vertical structure of the free troposphere is a reduced-gravity layer, a choice in midlatitudes that excludes vertically propagating waves (e.g., Kilpatrick et al. 2014) and interactions of the boundary layer with the evolution of potential vorticity in the free troposphere considered in Feliks et al. (2004, 2007, 2011). This simplified vertical structure, however, is a conceptual prototype to show the similarity of the boundary layer response to the classical Rossby adjustment and to determine the impact on the coupling coefficients, and is best suited to stratocumulus regimes (Schubert et al. 1979b). The model is formulated on a midlatitude f plane and cannot explain directly observations of $\alpha_D > \alpha_C$ of the low-latitude eastern Pacific (Chelton et al. 2004). On the other hand, the lateral shear of trades may provide sufficient relative vorticity to retain the essential dynamics described here, a hypothesis consistent with a momentum balance between background advection, vertical mixing, and pressure gradient forces found in simulations of lower atmospheric response to tropical instability waves (Small et al. 2003). The development of shallow, internal boundary layers in temperature downstream of a warm-to-cold SST transition (Kilpatrick et al. 2014) is not included in the heat budget. It is left to future studies to relax these assumptions and include a vertically dependent heat budget and moist processes, and to couple the boundary layer model to continuously stratified troposphere that allows vertically propagating gravity waves and interactions with the dynamics of the free troposphere, as in Brachet et al. (2012).

Given the vigorous atmospheric synoptic variability in the midlatitude regions of large SST gradients of the western boundary currents and Southern Ocean, the accuracy of the linear approximation of our model may be limited, and it remains to be seen if analyses of observations or high-resolution models confirm its relevance. However, the linear dynamics discussed here provide a unified framework that we hope is useful for future studies of frontal air–sea interaction.

Acknowledgments. This work has benefited from discussions with Drs. Jessica Benthuysen, Thomas Kilpatrick, Emanuele Di Lorenzo, Shoshiro Minobe, Masami Nonaka, Larry O'Neill, Jim Potemra, Yoshi Sasaki, Justin Small, Bunmei Taguchi, Kohei Takatama, Axel Timmermann, Hiroki Tokinaga, and Shang-Ping Xie. Thoughtful comments by Drs. Larry O'Neill, Hisashi Nakamura, Mr. Ryusuke Masunaga, and an anonymous reviewer greatly improved an earlier draft of this manuscript. We gratefully acknowledge support by National Science Foundation (Grants OCE06-47994, OCE13-57157, and OCE09-26594); by the Department of Energy, Office of Science (Grants DOE-SC0006766 and DOE DE-SC0005111); by the National Aeronautics and Space Administration (Grant NNX14AL83G); and by the Japan Agency for Marine-Earth Science and Technology as part of the JAMSTEC–IPRC Joint Investigations (JIJI).

APPENDIX

Derivation of the Nondimensional Reduced-Gravity Model

The horizontal momentum balance, in steady state and driven by a prescribed geostrophic wind $\mathbf{U}_g$, is

$$\mathbf{u}\cdot\nabla\mathbf{u} + w\partial_z\mathbf{u} + f\hat{\mathbf{e}}_3\times(\mathbf{u}-\mathbf{U}_g) = -\rho^{-1}\nabla p + \partial_z A\partial_z\mathbf{u}, \tag{A1}$$

where all variables carry units, $\mathbf{u}$ is the horizontal velocity vector, w is the vertical component of the velocity, ∇ acts in the horizontal only, f is the Coriolis frequency, $\hat{\mathbf{e}}_3$ is the unit vector in the vertical, ρ is the density, p is

TABLE A1. Scales used in the nondimensionalization.

Variable		Scale
$\mathbf{x}$	$\sqrt{g'H}/f$	Rossby radius of deformation
s	1	
h	H	Mean inversion height
$\mathbf{u}$	$\sqrt{g'H}$	Gravity wave speed
$w^\star$	Hf	
Θ, T	$\Delta\Theta$	Mean inversion strength

the pressure, A is the vertical exchange coefficient, and z is the vertical coordinate. For a 1.5-layer reduced-gravity framework, Θ_0 is the vertically constant potential temperatures of the passive troposphere above the sharp inversion at $z = h$, and $\Theta_0 - \Delta\Theta + \Theta$ is the vertically constant potential temperature in the active lower layer below, with $\Delta\Theta$ the mean strength of the inversion, and Θ the perturbation potential temperature. The horizontal gradient of the hydrostatic pressure gradient then reads

$$\rho^{-1}\nabla p = g'\left(1-\frac{\Theta}{\Delta\Theta}\right)\nabla h - g'h\frac{1}{1-\dfrac{\Delta\Theta}{\Theta_0}\left(1-\dfrac{\Theta}{\Delta\Theta}\right)}\left(1-\frac{z}{h}\right)\nabla\frac{\Theta}{\Delta\Theta}, \quad \text{(A2)}$$

where $g' = (\Delta\Theta/\Theta_0)g$ is the reduced gravity, and g is Earth's gravitational acceleration.

The continuity equation is

$$\nabla\cdot\mathbf{u} + \partial_z w = 0. \quad \text{(A3)}$$

After changing the vertical coordinate from z to sigma levels $s = z/h$ and neglecting the term proportional to $\Delta\Theta/\Theta_0$ in the classical Boussinesq approximation, the momentum and continuity equations read

$$\mathbf{u}\cdot\nabla\mathbf{u} + w^\star\partial_s\mathbf{u} + f\hat{\mathbf{e}}_3\times(\mathbf{u}-\mathbf{U}_g) = -g'\left(1-\frac{\Theta}{\Delta\Theta}\right)\nabla h + g'h(1-s)\nabla\frac{\Theta}{\Delta\Theta} + h^{-2}\partial_s A\partial_s\mathbf{u} \quad \text{and} \quad \text{(A4)}$$

$$\nabla\cdot\mathbf{u} + h^{-1}\mathbf{u}\cdot\nabla h + h^{-1}\partial_s w^\star = 0, \quad \text{(A5)}$$

which become, after being nondimensionalized using the scales in Table A1, Eqs. (2) and (5), with forcing $\mathbf{U}_g/\sqrt{g'H}$ and Ekman number $E = A/(fH^2)$ as sole coefficients.

REFERENCES

Battisti, D., E. Sarachik, and A. Hirst, 1999: A consistent model for the large-scale steady surface atmospheric circulation in the tropics. *J. Climate,* **12,** 2956–2964, doi:10.1175/1520-0442(1999)012<2956:ACMFTL>2.0.CO;2.

Bellon, G., and B. Stevens, 2013: Time scales of the trade wind boundary layer adjustment. *J. Atmos. Sci.,* **70,** 1071–1083, doi:10.1175/JAS-D-12-0219.1.

Benthuysen, J., 2010: Linear and nonlinear stratified spindown over sloping topography. Ph.D. thesis, Massachusetts Institute of Technology and Woods Hole Oceanographic Institution, 205 pp. [Available online at http://hdl.handle.net/1721.1/59740.]

Betts, A. K., 1989: Mean inversion strength of the convective boundary layer over the oceans. *Quart. J. Roy. Meteor. Soc.,* **115,** 997–998, doi:10.1002/qj.49711548812.

Brachet, S., F. Codron, Y. Feliks, M. Ghil, H. Le Treut, and E. Simonnet, 2012: Atmospheric circulations induced by a midlatitude SST front: A GCM study. *J. Climate,* **25,** 1847–1853, doi:10.1175/JCLI-D-11-00329.1.

Bryan, F., R. Tomas, J. Dennis, D. Chelton, N. Loeb, and J. McClean, 2010: Frontal scale air–sea interaction in high-resolution coupled climate models. *J. Climate,* **23,** 6277–6291, doi:10.1175/2010JCLI3665.1.

Businger, J., and W. Shaw, 1984: The response of the marine boundary layer to mesoscale variations in sea-surface temperature. *Dyn. Atmos. Oceans,* **8,** 267–281, doi:10.1016/0377-0265(84)90012-5.

Chelton, D. B., and S. Xie, 2010: Coupled ocean–atmosphere interaction at oceanic mesoscales. *Oceanography,* **23,** 52–69, doi:10.5670/oceanog.2010.05.

——, M. G. Schlax, M. H. Freilich, and R. F. Milliff, 2004: Satellite measurements reveal persistent small-scale features in ocean winds. *Science,* **303,** 978–983, doi:10.1126/science.1091901.

Cronin, M., and W. Kessler, 2009: Near-surface shear flow in the tropical Pacific cold tongue front. *J. Phys. Oceanogr.,* **39,** 1200–1215, doi:10.1175/2008JPO4064.1.

Feliks, Y., M. Ghil, and E. Simonnet, 2004: Low-frequency variability in the midlatitude atmosphere induced by an oceanic thermal front. *J. Atmos. Sci.,* **61,** 961–981, doi:10.1175/1520-0469(2004)061<0961:LVITMA>2.0.CO;2.

——, ——, and ——, 2007: Low-frequency variability in the midlatitude baroclinic atmosphere induced by an oceanic thermal front. *J. Atmos. Sci.,* **64,** 97–116, doi:10.1175/JAS3780.1.

——, ——, and A. Robertson, 2011: The atmospheric circulation over the North Atlantic as induced by the SST field. *J. Climate,* **24,** 522–542, doi:10.1175/2010JCLI3859.1.

Frenger, I., N. Gruber, R. Knutti, and M. Münnich, 2013: Imprint of Southern Ocean eddies on winds, clouds and rainfall. *Nat. Geosci.,* **6,** 608–612, doi:10.1038/ngeo1863.

Gill, A. E., 1982: *Atmosphere–Ocean Dynamics.* International Geophysics Series, Vol. 30, Academic Press, 662 pp.

Greenspan, H., and L. Howard, 1963: On a time-dependent motion of a rotating fluid. *J. Fluid Mech.,* **17,** 385–404, doi:10.1017/S0022112063001415.

Hashizume, H., S.-P. Xie, M. Fujiwara, M. Shiotani, T. Watanabe, Y. Tanimoto, W. T. Liu, and K. Takeuchi, 2002: Direct observations of atmospheric boundary layer response to SST variations associated with tropical instability waves over the eastern equatorial Pacific. *J. Climate,* **15,** 3379–3393, doi:10.1175/1520-0442(2002)015<3379:DOOABL>2.0.CO;2.

Hayes, S., M. McPhaden, and J. Wallace, 1989: The influence of sea-surface temperature on surface wind in the eastern equatorial Pacific: Weekly to monthly variability. *J. Climate,* **2,** 1500–1506, doi:10.1175/1520-0442(1989)002<1500:TIOSST>2.0.CO;2.

Holton, J. R., 1965a: The influence of viscous boundary layers on transient motions in a stratified rotating fluid. Part I. *J. Atmos. Sci.,* **22,** 402–411, doi:10.1175/1520-0469(1965)022<0402:TIOVBL>2.0.CO;2.

——, 1965b: The influence of viscous boundary layers on transient motions in a stratified rotating fluid. Part II. *J. Atmos. Sci.,* **22,** 535–540, doi:10.1175/1520-0469(1965)022<0535:TIOVBL>2.0.CO;2.

Hong, S.-Y., and H.-L. Pan, 1996: Nonlocal boundary layer vertical diffusion in a medium-range forecast model. *Mon. Wea. Rev.,* **124,** 2322–2339, doi:10.1175/1520-0493(1996)124<2322:NBLVDI>2.0.CO;2.

Kilpatrick, T., 2013: A modeling study of the atmospheric response to a midlatitude SST front. Ph.D. thesis, University of Hawai'i at Mānoa, 107 pp.

——, N. Schneider, and B. Qiu, 2014: Boundary layer convergence induced by strong winds across a midlatitude SST front. *J. Climate,* **27,** 1698–1718, doi:10.1175/JCLI-D-13-00101.1.

Koseki, S., and M. Watanabe, 2010: Atmospheric boundary layer response to mesoscale SST anomalies in the Kuroshio Extension. *J. Climate,* **23,** 2492–2507, doi:10.1175/2009JCLI2915.1.

Lambaerts, J., G. Lapeyre, R. Plougonven, and P. Klein, 2013: Atmospheric response to sea surface temperature mesoscale structures. *J. Geophys. Res. Atmos.,* **118,** 9611–9621, doi:10.1002/jgrd.50769.

Lindzen, R., and S. Nigam, 1987: On the role of sea surface temperature gradients in forcing low-level winds and convergence in the tropics. *J. Atmos. Sci.,* **44,** 2418–2436, doi:10.1175/1520-0469(1987)044<2418:OTROSS>2.0.CO;2.

MacCready, P., and P. Rhines, 1991: Buoyant inhibition of Ekman transport on a slope and its effect on stratified spin-up. *J. Fluid Mech.,* **223,** 631–661, doi:10.1017/S0022112091001581.

Minobe, S., M. Miyashita, A. Kuwano-Yoshida, H. Tokinaga, and S. Xie, 2010: Atmospheric response to the Gulf Stream: Seasonal variations. *J. Climate,* **23,** 3699–3719, doi:10.1175/2010JCLI3359.1.

Niino, H., 1987: The linear theory of land and sea breeze circulation. *J. Meteor. Soc. Japan,* **65,** 901–921.

O'Neill, L. W., D. B. Chelton, and S. K. Esbensen, 2003: Observations of SST-induced perturbations of the wind stress field over the Southern Ocean on seasonal timescales. *J. Climate,* **16,** 2340–2354, doi:10.1175/2780.1.

——, ——, and ——, 2010a: The effects of SST-induced surface wind speed and direction gradients on midlatitude surface vorticity and divergence. *J. Climate,* **23,** 255–281, doi:10.1175/2009JCLI2613.1.

——, S. K. Esbensen, N. Thum, R. Samelson, and D. B. Chelton, 2010b: Dynamical analysis of the boundary layer and surface wind responses to mesoscale SST perturbations. *J. Climate,* **23,** 559–581, doi:10.1175/2009JCLI2662.1.

——, D. B. Chelton, and S. K. Esbensen, 2012: Covariability of surface wind and stress responses to sea surface temperature fronts. *J. Climate,* **25,** 5916–5942, doi:10.1175/JCLI-D-11-00230.1.

Park, K., P. Cornillon, and D. Codiga, 2006: Modification of surface winds near ocean fronts: Effects of Gulf Stream rings on scatterometer (QuikSCAT, NSCAT) wind observations. *J. Geophys. Res.,* **111,** C03021, doi:10.1029/2005JC003016.

Pedlosky, J., 1967: The spin up of a stratified fluid. *J. Fluid Mech.,* **28,** 463–479, doi:10.1017/S0022112067002228.

Rotunno, R., 1983: On the linear theory of the land and sea breeze. *J. Atmos. Sci.,* **40,** 1999–2009, doi:10.1175/1520-0469(1983)040<1999:OTLTOT>2.0.CO;2.

Samelson, R., E. Skyllingstad, D. Chelton, S. Esbensen, L. O'Neill, and N. Thum, 2006: On the coupling of wind stress and sea surface temperature. *J. Climate,* **19,** 1557–1566, doi:10.1175/JCLI3682.1.

Schubert, W. H., J. S. Wakefield, E. J. Steiner, and S. K. Cox, 1979a: Marine stratocumulus convection. Part I: Governing equations and horizontally homogeneous solutions. *J. Atmos. Sci.,* **36,** 1286–1307, doi:10.1175/1520-0469(1979)036<1286:MSCPIG>2.0.CO;2.

——, ——, ——, and ——, 1979b: Marine stratocumulus convection. Part II: Horizontally inhomogeneous solutions. *J. Atmos. Sci.,* **36,** 1308–1324, doi:10.1175/1520-0469(1979)036<1308:MSCPIH>2.0.CO;2.

Seo, H., A. J. Miller, and J. O. Roads, 2007: The Scripps Coupled Ocean–Atmosphere Regional (SCOAR) model, with applications in the eastern Pacific sector. *J. Climate,* **20,** 381–402, doi:10.1175/JCLI4016.1.

Shimada, T., and S. Minobe, 2011: Global analysis of the pressure adjustment mechanism over sea surface temperature fronts using AIRS/Aqua data. *Geophys. Res. Lett.,* **38,** L06704, doi:10.1029/2010GL046625.

Small, R. J., S.-P. Xie, and Y. Wang, 2003: Numerical simulation of atmospheric response to Pacific tropical instability waves. *J. Climate,* **16,** 3723–3741, doi:10.1175/1520-0442(2003)016<3723:NSOART>2.0.CO;2.

——, ——, ——, S. K. Esbensen, and D. Vickers, 2005: Numerical simulation of boundary layer structure and cross-equatorial flow in the eastern Pacific. *J. Atmos. Sci.,* **62,** 1812–1830, doi:10.1175/JAS3433.1.

——, and Coauthors, 2008: Air–sea interaction over ocean fronts and eddies. *Dyn. Atmos. Oceans,* **45,** 274–319, doi:10.1016/j.dynatmoce.2008.01.001.

Song, Q., D. Chelton, S. Esbensen, N. Thum, and L. O'Neill, 2009: Coupling between sea surface temperature and low-level winds in mesoscale numerical models. *J. Climate,* **22,** 146–164, doi:10.1175/2008JCLI2488.1.

Spall, M., 2007: Midlatitude wind stress–sea surface temperature coupling in the vicinity of oceanic fronts. *J. Climate,* **20,** 3785–3801, doi:10.1175/JCLI4234.1.

Stull, R. B., 1988: *An Introduction to Boundary Layer Meteorology.* Atmospheric Sciences Library, Vol. 13, Kluwer Academic Publishers, 666 pp.

Suzuki, S.-I., H. Niino, and R. Kimura, 2011: The mechanism of upper-oceanic vertical motions forced by a moving typhoon. *Fluid Dyn. Res.,* **43,** 025504, doi:10.1088/0169-5983/43/2/025504.

Sweet, W., R. Fett, J. Kerling, and P. La Violette, 1981: Air–sea interaction effects in the lower troposphere across the north wall of the Gulf Stream. *Mon. Wea. Rev.,* **109,** 1042–1052, doi:10.1175/1520-0493(1981)109<1042:ASIEIT>2.0.CO;2.

Takatama, K., S. Minobe, M. Inatsu, and R. J. Small, 2012: Diagnostics for near-surface wind convergence/divergence response to the Gulf Stream in a regional atmospheric model. *Atmos. Sci. Lett.,* **13,** 16–21, doi:10.1002/asl.355.

Tokinaga, H., Y. Tanimoto, S.-P. Xie, T. Sampe, H. Tomita, and H. Ichikawa, 2009: Ocean frontal effects on the vertical development of clouds over the western North Pacific: In situ and satellite observations. *J. Climate,* **22,** 4241–4260, doi:10.1175/2009JCLI2763.1.

Wai, M., and S. A. Stage, 1989: Dynamical analysis of marine atmospheric boundary layer structure near the Gulf Stream oceanic front. *Quart. J. Roy. Meteor. Soc.,* **115,** 29–44, doi:10.1002/qj.49711548503.

Wallace, J., T. Mitchell, and C. Deser, 1989: The influence of sea-surface temperature on surface wind in the eastern equatorial Pacific: Seasonal and interannual variability. *J. Climate,* **2,** 1492–1499, doi:10.1175/1520-0442(1989)002<1492:TIOSST>2.0.CO;2.

Xie, S.-P., 2004: Satellite observations of cool ocean–atmosphere interaction. *Bull. Amer. Meteor. Soc.,* **85,** 195–208, doi:10.1175/BAMS-85-2-195.